ATL-TILECAL-PUB-2005-003
15 April 2005

Electromagnetic Energy Calibration of the TILECAL Modules with the Flat Filter Method (July 2002 Test Beam Data)

J.A. Budagov[1], J.I. Khubua[1], Y.A. Kulchitsky[1, 2], N.A. Russakovich[1], P.V. Tsiareshka[1, 2], V.B. Vinogradov[1]

[1)] *JINR, Dubna, Russia,*
[2)] *IP National Academy of Sciences, Minsk, Belarus*

Abstract

The constructed ATLAS detector at the LHC will have the great physics discovery potential, in particular in the detection of a heavy Higgs boson. Calorimeters will play a crucial role in it. The important question of calorimetry is the calibration in the electromagnetic energy scale.

With the aim of establishing of this scale and understanding of performance of the ATLAS Tile hadronic calorimeter to electrons 12% of modules have been exposed in electron beams with various energies by three possible ways: cell-scan at $\theta = 20^o$ at the centers of the front face cells, η-scan and tilerow scan at $\theta = 90^o$ for the module side cells.

Our work is devoted to the determination of the electromagnetic energy calibration constants of the EBM− (ANL-44), EBM+ (IFA-42), BM (JINR-55) TILECAL modules at energies E = 10, 20, 50, 100 and 180 GeV and $\theta = 20^o$ and 90^o and η scans on the basis of the July 2002 testbeam run data using the flat filter method of the PMT signal reconstruction.

The obtained average electron calibration constants equal to $\langle R_e \rangle = 1.157 \pm 0.002$, $RMS = 2.6 \pm 0.2\%$ for $\theta = 20^o$, $\langle R_e \rangle = 1.196 \pm 0.005$, $RMS = 5.7 \pm 0.3\%$ for $\theta = 90^o$ and $\langle R_e \rangle = 1.143 \pm 0.005$, $RMS = 3.7 \pm 0.3\%$ for η- scan.

The obtained calibration constants have been included in the TILECAL calibration database and will be used for the energy calibration of all TILECAL modules.

1 Introduction

The constructed ATLAS detector at the LHC will have the great physics discovery potential, in particular in the detection of a heavy Higgs boson [1, 2]. Calorimeters will play a crucial role in it. The key question of calorimetry is the absolute energy calibration,in particular he calibration in the electromagnetic energy scale.

The physics goals have led to the following requirement for the knowledge of the absolute scale of energy: in the case of hadronic jets, the scale should be known to an accuracy of 1% [3].

The other important issue is the energy linearity. The most stringent linearity requirements for the hadronic calorimeter come from the study of quark compositeness where the jet energy scale has to be linear within 1.5% up to the transverse energy of 4 TeV [2, 4].

For each cell of the ATLAS hadronic TILECAL calorimeter [5] the calibration constants, which define the relationship between the calorimeter signals, expressed in picoCoulombs, and the energy of the absorbed particles, which produced the signals, must be determined. The calibration constants depend on the type of particle, or jet and, generally speaking, on their energies [6]. This means that calibration constants determined for one particular type of particle, or jet of one particular energy lead to systematic mismeasurements of energy if used for the interpretation of signals caused by other particles, or jets of other energies.

Among the possible energy scales the electromagnetic energy scale has a great attraction due to a very fundamental calorimeter property which is signal linearity for electromagnetic showers since the entire electromagnetic shower energy is used to ionize and excite the molecules of which the calorimeter consists. Twice as much energy thus leads to twice as many excited and ionized molecules and should thus leads to calorimeter signals that are twice as large [6].

It is assumed that for the ATLAS calorimeters the hadronic final states physics objects (hadrons, jets, missing transverse energy) should be reconstructed at first using calorimeter signals on an electromagnetic energy scale [7, 8].

With the aim of establishing of the electromagnetic energy scale and understanding of performance of the ATLAS Tile calorimeter to electrons 12% of modules have been exposed in electron beams with various energies by three possible ways: cell-scan at $\theta = 20^o$ at the centers of the

front face cells, η scan (η is a pseudorapidity, $\eta = -\ln\tan((90^o - \theta)/2)$ in the case of the test beam setup) and tilerow scan at $\theta = 90^o$ for the module side cells.

This work is devoted to the determination of the electron calibration constants of the ATLAS iron-scintillator tile hadron calorimeter modules JINR-55, IFA-42 and ANL-44 on the basis of the July 2002 test beam period using the flat filter method of the PMT signal reconstruction.

Earlier we have performed the electromagnetic calibration for a number of modules [9, 10, 11].

2 The ATLAS Hadron Tile Calorimeter

The ATLAS Hadron Tile Calorimeter (TileCal) is a 2900 t sampling calorimeter using iron as passive material and tiles of scintillator as active material readout by wavelength shifting fibers [5]. This calorimeter will play a very important role to identify jets, measure their energy and direction, reconstruct the transverse missing energy. The goal of the TileCal is to measure hadrons energy with good resolution ($\sigma/E = 50\%\sqrt{GeV}/\sqrt{E} \oplus 3\%$) and linearity (1-2 % up to TeV scale).

An innovative feature of this calorimeter is the orientation of the scintillators that are placed in planes perpendicular to the colliding beams (Fig. 1 (left)). This disposition simplifies the tile-fiber and fiber-PMT coupling reducing the dead spaces of the calorimeter and hence increasing hermecity. Due to this feature we can get an hermetic coverage up to $|\ \eta\ | = 1.7$ ($|\ \eta\ | = 5$ with forward calorimeters), very important for the reconstruction of the transverse missing energy.

The TileCal is divided into one barrel and two extended barrel sections. All three sections have a cylindrical structure with an inner radius of 2280 mm and outer one of 4230 mm. The barrel section is 5460 mm in length along the beam axis, while each extended barrel has a length of about 2910 mm. Each of the cylinders is further subdivided into 64 independent azimuthally oriented modules. Within each module, there are a number of readout cells. Each cell is a set of scintillating tiles connected by fibers to 2 PMTs. The TileCal will contain 4672 cells which will be read-out by 9344 PMTs. Two fibres collect light from every scintillator tile at both of its azimuthal edges. The total number of tiles is 456000. In this way the calorimeter is divided in η towers, which are "pseudo-projective" towards the interaction region, and radially seg-

mented in three depths. The thicknesses of depths at η=0 are 1.5 λ in the first sampling, 4.2 λ in the second one, and 1.9 λ in the third one, with a total depth of 7.6 λ. The granularity $\Delta\eta \times \Delta\varphi$ at η=0 is 0.1×0.1 for the first two depths and 0.2×0.1 in the third compartment.

The iron structure of each module consists of a number of repeated periods (Fig. 1 (right)). Each period is 18 mm thick and consists of four layers. The first and third layers are formed by large trapezoidal steel plates (master plates), and spanning the full longitudinal dimension of the module. In the second and fourth layers, smaller trapezoidal steel plates (spacer plates) and scintillator tiles alternate. These layers consist of 11 different trapezoids of steel and scintillator, each spanning from 97 to 187 mm. The master plates, spacer plates and scintillator tiles are of 5 mm, 4 mm and 3 mm thick, respectively. The iron to scintillator ratio is 4.67:1 by volume.

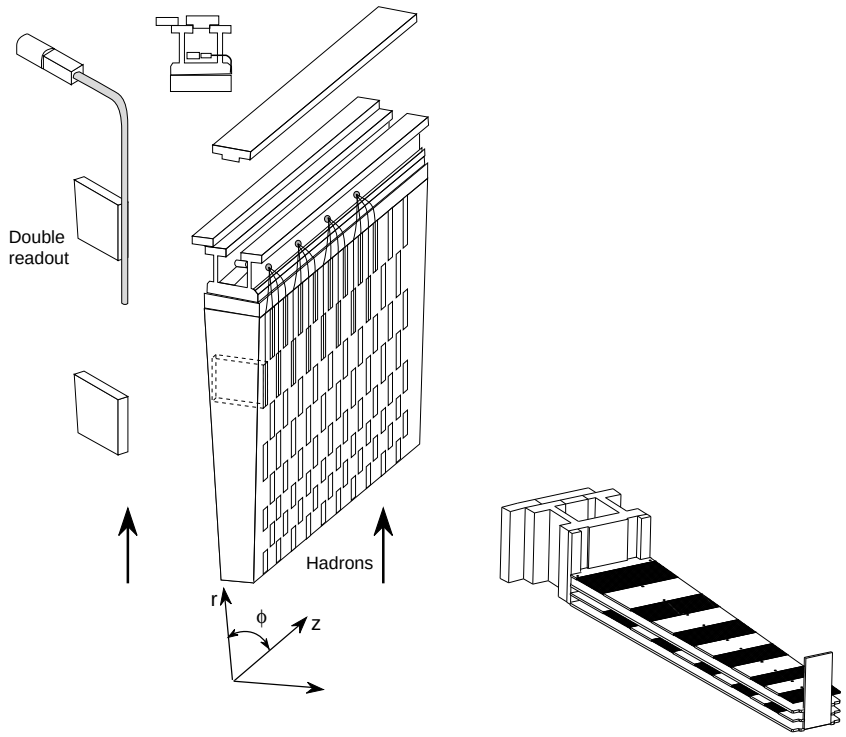

Figure 1: Principle of the TileCal (left). Exploded view of an assembled TileCal period (right).

3 Test beam setup

The test beam setup used for the calibration is the following (Fig. 2).

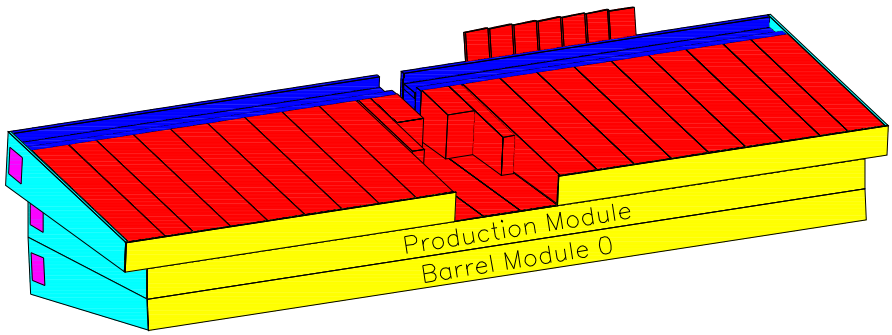

Figure 2: Sketch of the July 2002 test beam setup. Barrel module JINR-55 is the middle layer. Extended Barrel modules IFA-42 $\eta > 0$ (beam left) and ANL-44 $\eta < 0$ (beam right) are the top layer.

The Barrel Module 0 is the bottom module mounted on the table. The middle layer is the production barrel module BM$\pm$ (JINR-55). The top layer is the two extended barrel modules: EBM+ (IFA-42) for $\eta > 0$ (beam left) and EBM$-$ (ANL-44) for $\eta < 0$ (beam right). Bad PMT channel is 9 connected with the A2 cell of the BM+.

The layout of the readout cell geometry for modules is shown in Fig. 3. Each module is read out in three longitudinal layers. The first layer consists of A-cells, the second one — of B- and C-cells, and the third one — of D-cells. There are 11 transverse rows of tiles (tilerows) in a module. For a barrel module A-cells have tilerows 1 – 3, B- and C-cells — 4 – 7, D-cells — 10 – 11.
For a extended barrel module A-cells have tilerows 1 – 3, B- and C-cells — 4 – 6, D-cells — 7 – 11.

The calibration program with electrons, pions and muons was performed in the H8 beam at the CERN SPS.

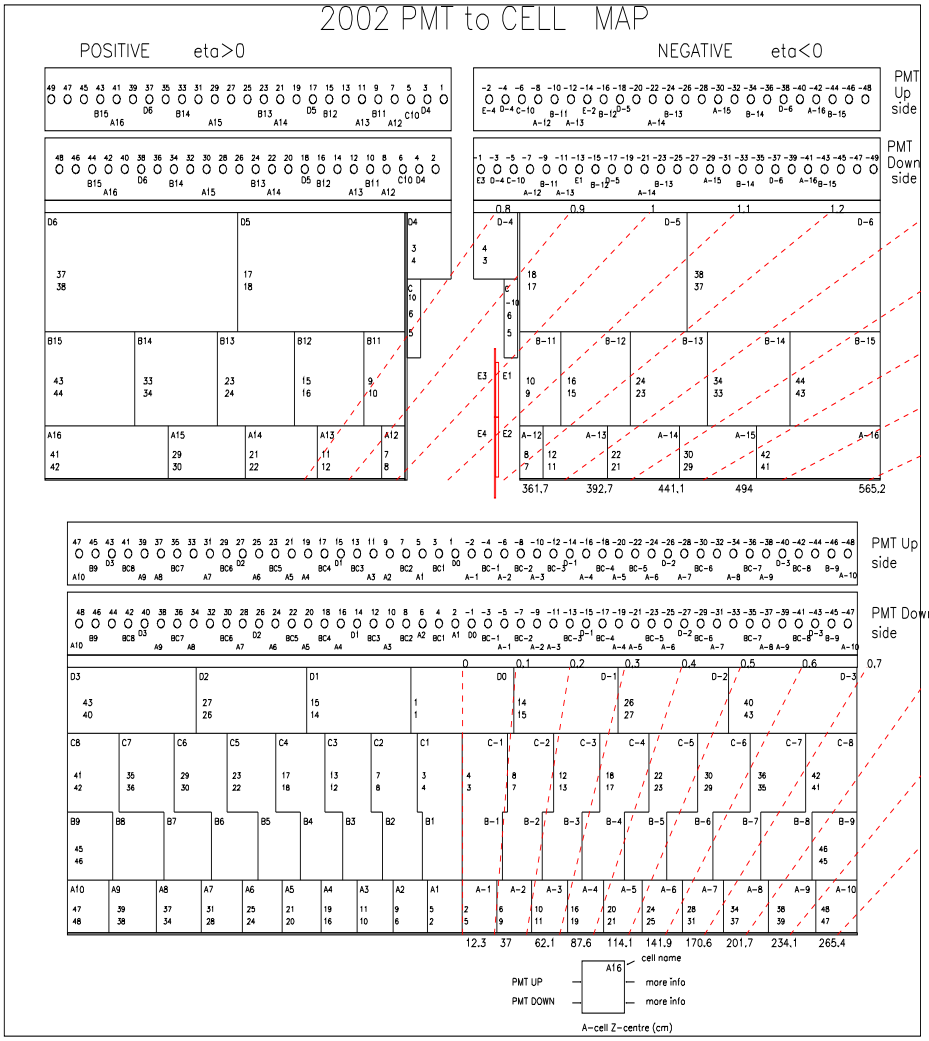

Figure 3: The layout of the cell geometry.

4 Data analysis

4.1 Data

We have used the July 2002 exposition of the setup by the electron beams with energies the 10, 20, 50, 100, 180 GeV at $\theta = \pm 20^o$, $\theta = 90^o$, $\eta = 0.05 \div 1.45$. The volume of the analyzed information is the following: 390 ntuples, 200 Gbyte, 15 million events.

4.2 Calibration volume

Since the electron calibration constants will be used for the hadron energy reconstruction [12, 13] we have summed the energy depositions in the cells inside of the cone with the radius $\Delta R = \sqrt{\Delta\phi^2 + \Delta\eta^2}$ in the pseudorapidity-azimuthal space. The value of ΔR is equal to 0.4 for single hadrons and 0.7 for jets [3, 14]. For the Tile calorimeter module $\Delta\phi$ is 0.1 and therefore for $\Delta R = 0.4$ we take $\Delta\eta = 0.4$. This corresponds to whole extended barrel module and half of barrel module (Fig. 3).

4.3 PMT signal reconstruction method

For the PMT signal reconstruction we have used the flat filter method [15, 16]. In this method the value of the PMT signal, R_{flat}, is an integral, a maximum of all possible sums of 5 subsequent samples of the pulse shape of a PMT signal which is sampled 9 times with the 25 ns interval

$$R_{flat} = C_{cis} \cdot \max \left(\sum_{i=j}^{j+4} (s_i - s_1) \right). \qquad (1)$$

The first sample (s_1) is considered as a pedestal and its value is subtracted from all other samples (s_i). Here C_{cis} is the constant transforming the ADC values into pC derived from CIS events, $j = 2, \ldots, 5$. As a consequence of finding the maximum, the flat filter method exhibits positive offset for the pedestal-like events. For majority of PMTs this offset, $\langle R_{noise} \rangle$, and RMS_{noise} do not exceed 0.016 pC and 0.06 pC, correspondingly, amounts to 0.01 pC and 0.05 pC, in average, as can be seen in Fig. 4. Besides, there are tails, 10% PMTs are with larger noise.

Such average positive offset for one PMT leads to the big total positive offset of about 0.4 GeV when summing all PMTs, for example, of half of

a barrel module and correspondingly to the 4% shift of the calibration constants at 10 GeV.

At using the method of cutting noise (in which the PMT channel signal is set equal to 0 if the value of signal less than Cut_{noise} value, with a typical value of 0.1 pC) the calibration constants at low energies (10 – 20 GeV) become dependent from a value of Cut_{noise} as shown in Fig. 4 (bottom). The data at high energy (180 GeV) are unsensitive to the value of Cut_{noise}, as expected.

We have devised the following algorithm excluding positive offset of the pedestal-like events. We analyze all signals in each channel of each event. If the value of some signal in i-channel less than $3 \cdot RMS_{noise,i}$ then this signal is decreased on the value of $\langle R_{noise,i} \rangle$. So, we obtain unshifted values of $\langle R_{noise,i} \rangle$.

4.4 Electrons selection

The H8 electron beams at the SPS CERN are the mixture of electrons, muons and hadrons. For calibration it is important to have the pure electron beam. We have estimated that in order to have the systematic error in the electron calibration constant due to the pion contamination smaller than 0.3 % this contamination must be smaller than 1.5 % in the energy range of 10 – 300 GeV [17].

Therefore, we have performed the identification of (e, μ, π) particles on the basis of the calorimetric information. We have used the following three selection criteria [17].

4.4.1 Electrons selection using longitudinal shower energy deposition

The first selection criterion

$$C_i = \sum_{selected\ i} \sum_{k=1}^{2} \sum_{l=1}^{2} E_{ikl}/E_{beam}, \qquad (2)$$

is a value of the relative shower energy deposition in the first two calorimeter depths, where E_{ikl} is the energy response of an ikl PMT, $[E_{ikl}] = pC$, k is a depth number, i is a cell number in the k-depth, $l = 1,\ 2$ is the PMT number in the ik cell, $[C_i] = pC/GeV$.

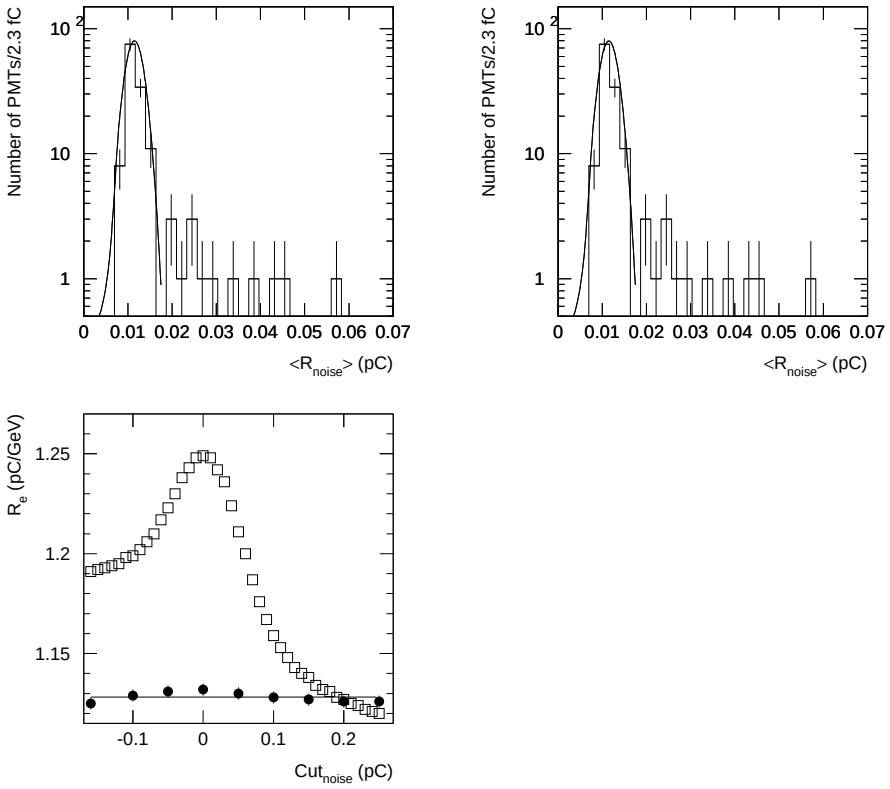

Figure 4: The distributions of mean values of PMT noise (top left) and RMS values (top right) of 142 PMTs used in the test beam July 2002 for the flat filter method (JINR-55, ANL-44, IFA-42). The electron calibration constants, R_e, for the A+1 cell of BM+ (JINR-55) at $\theta = 20^o$ for 10 (squares) and 180 (black points) GeV as a function of Cut_{noise} value (bottom). The peak values are $\langle R_{noise} \rangle$=10 MeV and RMS_{noise}=50 MeV.

The basis for this electron-hadron separation is the different longitudinal energy deposition for electrons and hadrons. For example, if a 100 GeV particle crosses 45 cm of the Tile calorimeter from the front face it corresponds to 18 radiation lengths or 2.2 nuclear interaction lengths. The amount of the deposited energy is equal to 95% for the electromagnetic shower and only 50% for the hadronic shower [18].

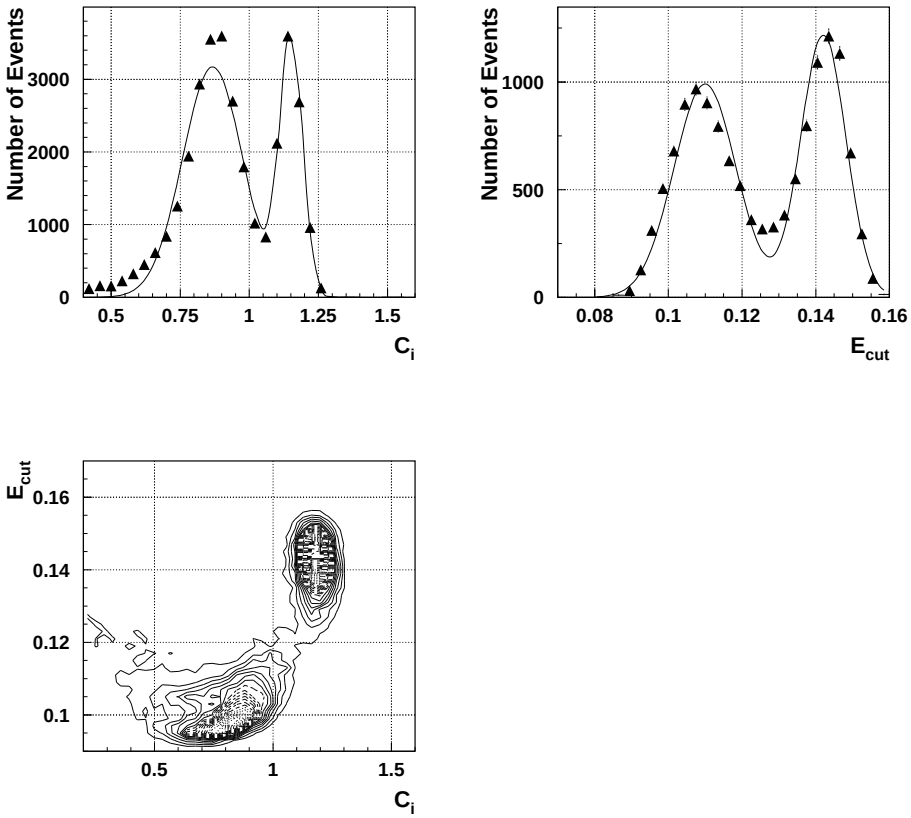

Figure 5: The C_i (left) and E_{cut} (center) distributions for 50 GeV and the scatter plot E_{cut} versus C_i (right) for 180 GeV.

Fig. 5 (left) shows the typical C_i distributions. The left peak corresponds to the pion events, the right peak corresponds to the electron events.

4.4.2 Electrons selection using lateral shower energy deposition

The second selection criterion is related with the lateral shower spread

$$E_{cut} = \frac{\sqrt{\sum_c (E_c^\alpha - \sum_c E_c^\alpha / N_{cell})^2}}{\sum_c E_c^\alpha} \ , \qquad (3)$$

where $1 \leq c \leq N_{cell}$, N_{cell} is the used cells number, $\alpha = 0.6$. For example, for the 100 GeV hadronic shower the 99% containment radius is equal to 430 mm, but for the electromagnetic shower the one is equal to 70 mm.

Fig. 5 (center) shows the typical E_{cut} distributions. The left peak corresponds to the pion events, the right peak corresponds to the electron events.

Fig. 5 (right) shows the scatter plot of E_{cut} versus C_i. The top right region are the electron events, the bottom left region are the pion events. These Figures allow to determine the values of the cuts and to estimate the contaminations.

We have estimated by extrapolation of the fitted pion peak curve to the region of the electron peak (Figs. 5) that the contamination of the pion events in the electron events does not exceed the 0.2% level.

4.4.3 Rejection of muons

For the muon rejection at energies $E_{beam} \geq 10GeV$ we have used the cut in the total deposited energy: $E_{tot} > E_{min}$ with $E_{min} = 5$ GeV [19]. This cut effectively selects muons as muons loose a very small fraction of their energy in the calorimeter.

4.4.4 Electrons selection using Cherenkov counter

At energies $\leq$ 20 GeV there is a bad selection of electrons by the C_i and E_{cut} criteria. This situation is greatly improved by using the first Cherenkov counter signal (cut 3).

Fig. 6 shows the typical scatter plots of E_{cut} versus $\check{\mathrm{C}}_1$ and C_i versus $\check{\mathrm{C}}_1$.

4.4.5 Resultant cuts

We have used the following three cuts for the electron selection [17]: the cut 1 is $C_i > 0.9 \div 1.1$, the cut 2 is $E_{cut} > 0.07 \div 0.14$, the cut 3 is

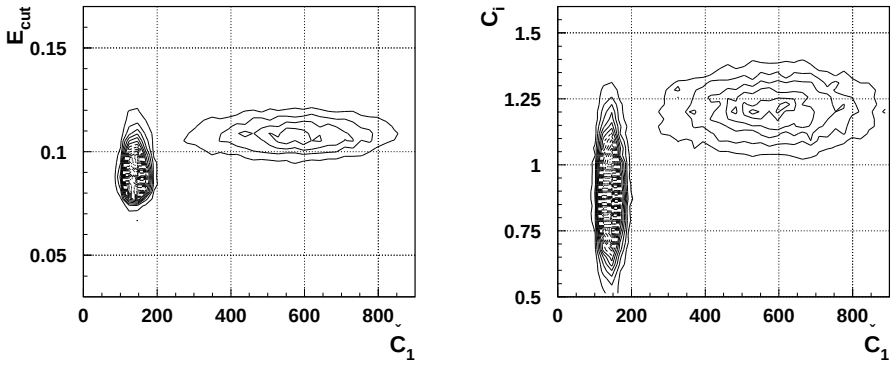

Figure 6: The scatter plots of E_{cut} vs $\check{\mathrm{C}}_1$ and C_i vs $\check{\mathrm{C}}_1$ for $E = 20\ GeV$, EBM+.

$\check{\mathrm{C}}_1 > 200 \div 400$.

Due to these cuts we have obtained the clean sample of the electron events for the calibration of modules of the TILECAL.

5 Tilecal electron response

The electron response in our calorimeter is a function of a beam energy, an incidence angle, an impact point [20].

The energy response spectrum for given run (beam has the transversal spread ± 15 mm) as a rule is non-Gaussian as can be seen in Fig. 7. The mean normalized electron responses as a function of an impact point Z coordinate for A-cells and η scans are described by the sine function (Fig. 8):

$$f(Z) = P_2 + P_1 \sin\left(2\pi Z/P_3 + P_4\right) . \qquad (4)$$

6 Electromagnetic Energy Calibration

The calibration constants (the mean normalized electron responses) have been extracted from the data of A-cell, tilerow and η scans and discuss in the following sections.

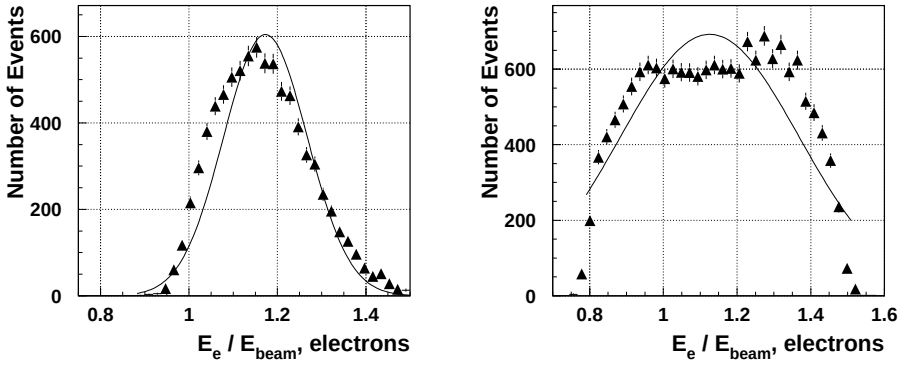

Figure 7: The relative electron energy distributions (pC/GeV) for BM+ for E = 10 GeV at $\theta = 20^o$ (left) and for BM− for $E = 20$ GeV at $\eta = -0.15$ (right).

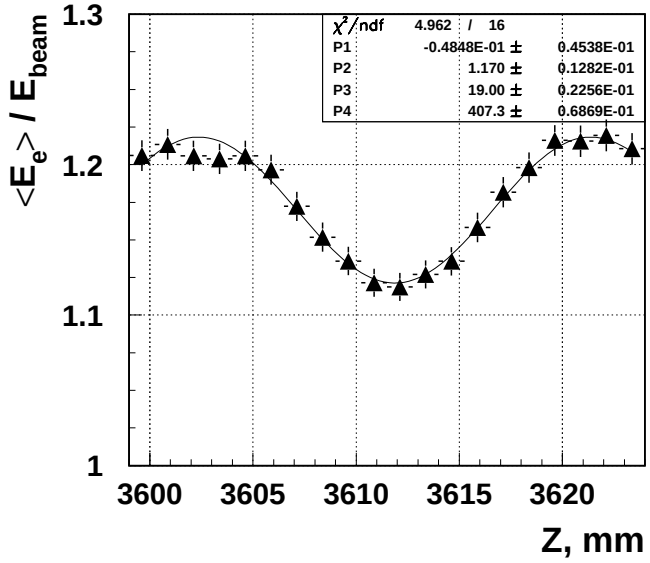

Figure 8: The normalized electron response (E_e/E_{beam}) for $E = 20\ GeV$ as a function of impact point Z coordinate.

6.1 A-cell scan at $\theta = 20^o$

Figs. 9–12 demonstrate the obtained calibration constants of EBM−, EBM+, BM−, BM+ modules at $\theta = 20^o$ for different energies as a function of A-cell number. The mean and RMS values are also shown. Tables 1–2 give the corresponding numerical values. Fig. 13 (down-right) show the distribution of the uniformity RMS values. As can be seen, uniformities of modules very vary, from 0.5% to 4%, with the mean value of $(2.1 \pm 0.2)\%$.

Fig. 13 shows the energy dependencies of the constants averaged over cells. Fig. 13 (down-left) gives the RMS values of energy non-linearity for separate modules. The mean RMS value is equal $(1.1 \pm 0.2)\%$. Fig. 14 shows the distributions of the calibration constants for $\theta = 20^o$ for all energies for EBM− , EBM+, BM− and BM+ separately, and for all modules together. The numerical values of means and RMS values of these distributions are given in Table 7.

The average value of the summary (three modules and five energies) distribution (Fig. 14 (down)) is equal to $\langle R_e \rangle = 1.157 \pm 0.002$ pC/GeV and $RMS = 2.6 \pm 0.2\%$.

6.2 η-scan

Figs. 15–17 show the obtained calibration constants for η-scan of EBM−, EBM+, BM−, BM+ modules for different energies as a function of η. Tables 3–4 give the corresponding numerical values. Fig. 18 (down-right) demonstrates the distribution of the uniformity RMS values. The mean value is equal to $(3.9 \pm 0.6)\%$. Fig. 18 (top, middle) shows the energy dependencies the constants averaged over cells. Fig. 18 (down-left) gives the RMS values of energy non-linearity for separate modules. The mean RMS value is equal $(1.3 \pm 0.3)\%$.

Fig. 19 demonstrates the distributions of the calibration constants for η-scan for all energies for EBM− , EBM+, BM− and BM+ modules separately, and for all modules together. The numerical values of means and RMS values of these distributions are given in Table 7. The average value of the summary distribution (Fig. 19 (left-down)) is equal to $\langle R_e \rangle = 1.143 \pm 0.005$ pC/GeV and $RMS = 3.7 \pm 0.3\%$ for all η values.

As can be seen from Figs. 15–17, big fluctuations in the values of calibration constants are observed for $\eta \leq 0.15$ ($\theta \leq 8.5^o$). Therefore, we have obtained the distribution of constants for $\eta > 0.15$ region (Fig. 19

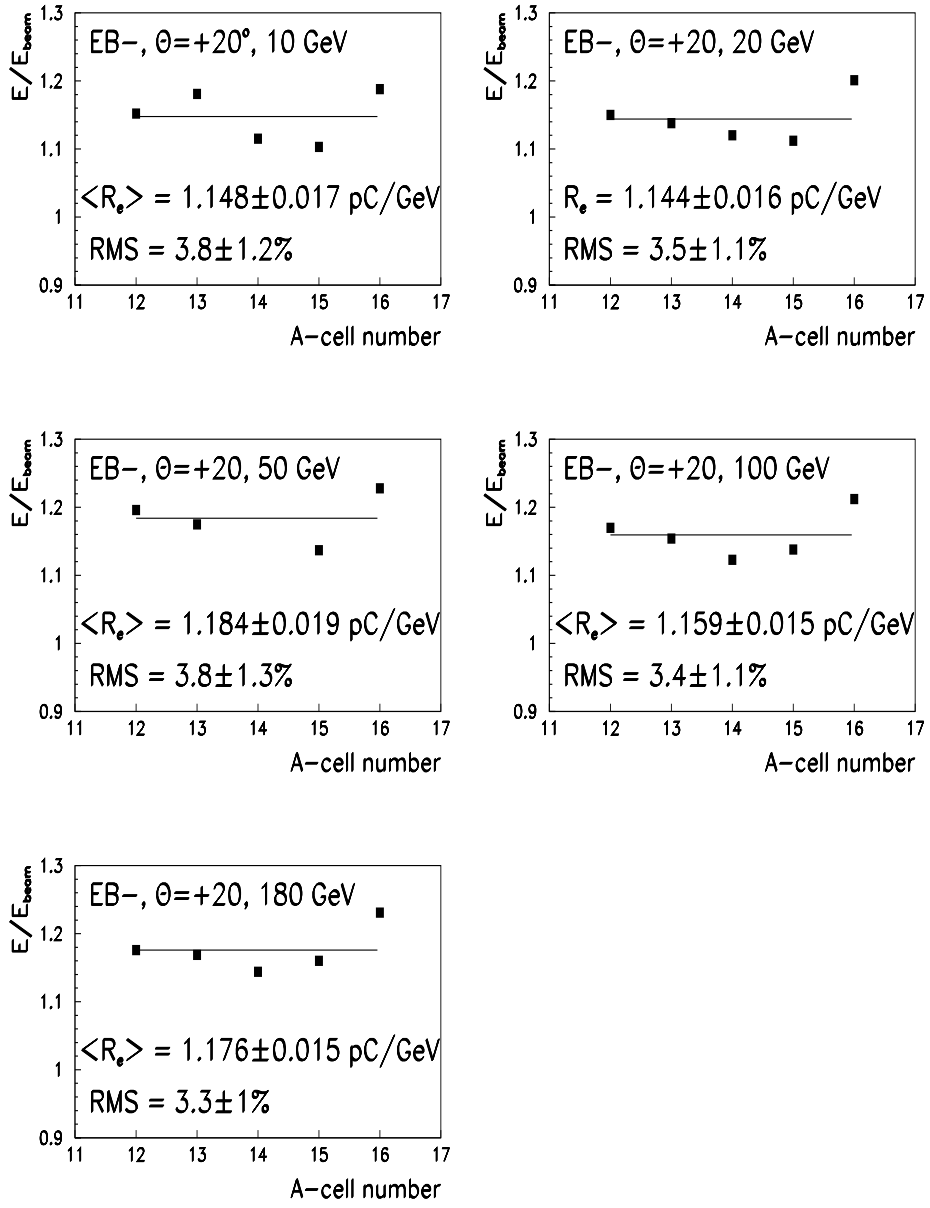

Figure 9: The calibration constants for the A-cells of EBM− for $\theta = 20^o$.

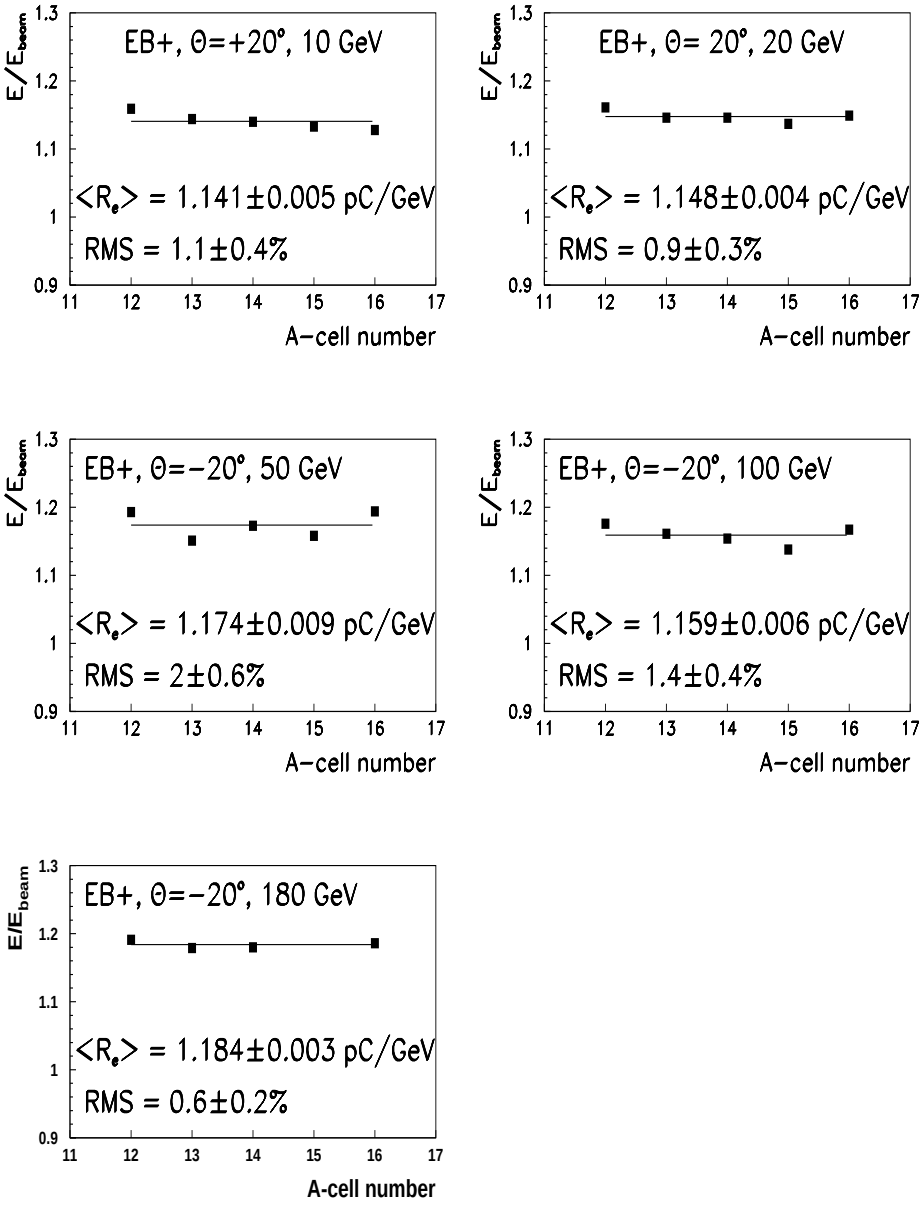

Figure 10: The calibration constants for the A-cells of EBM+ for $\theta = 20^o$.

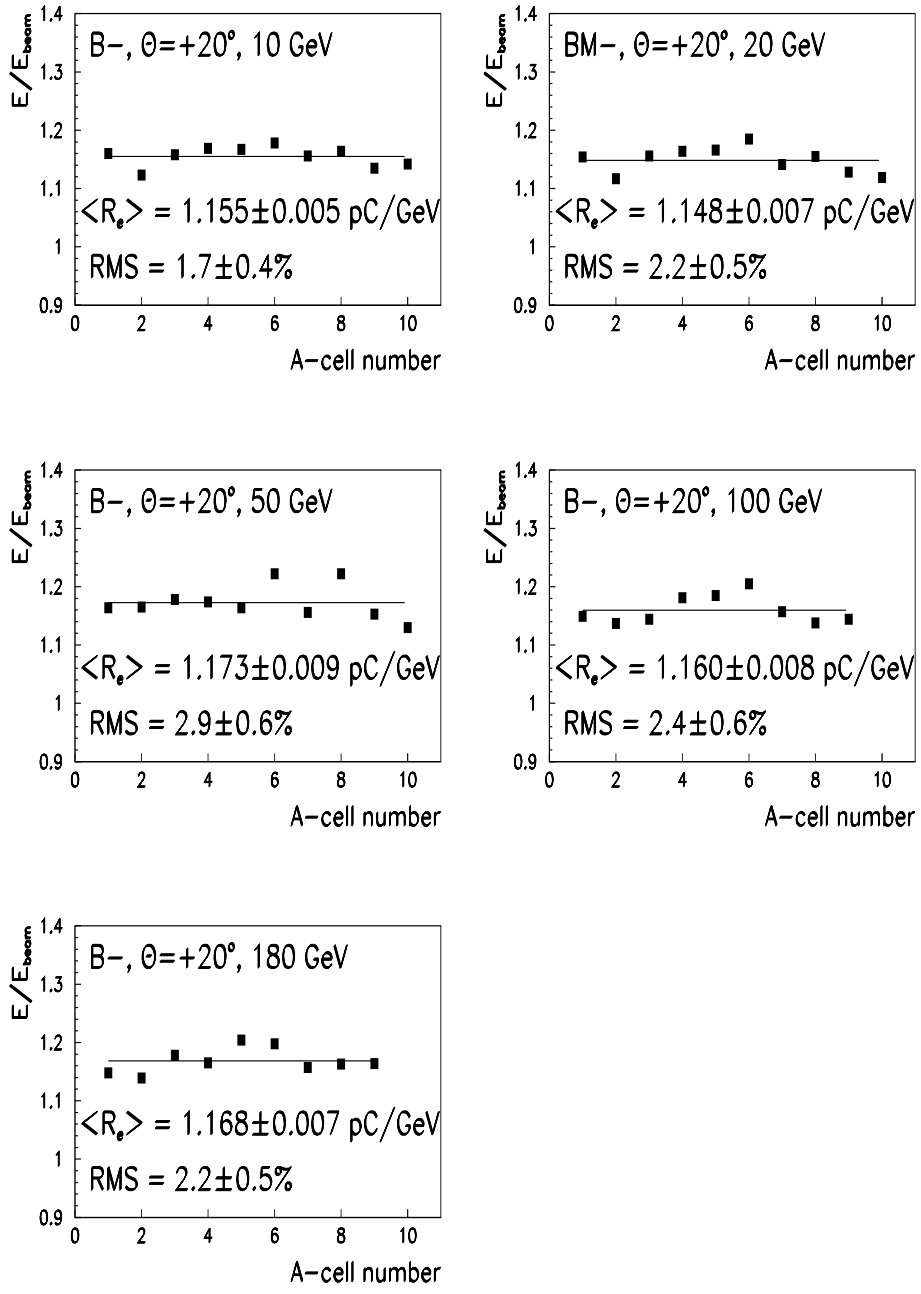

Figure 11: The calibration constants for the A-cells of BM− for $\theta = 20^{o}$.

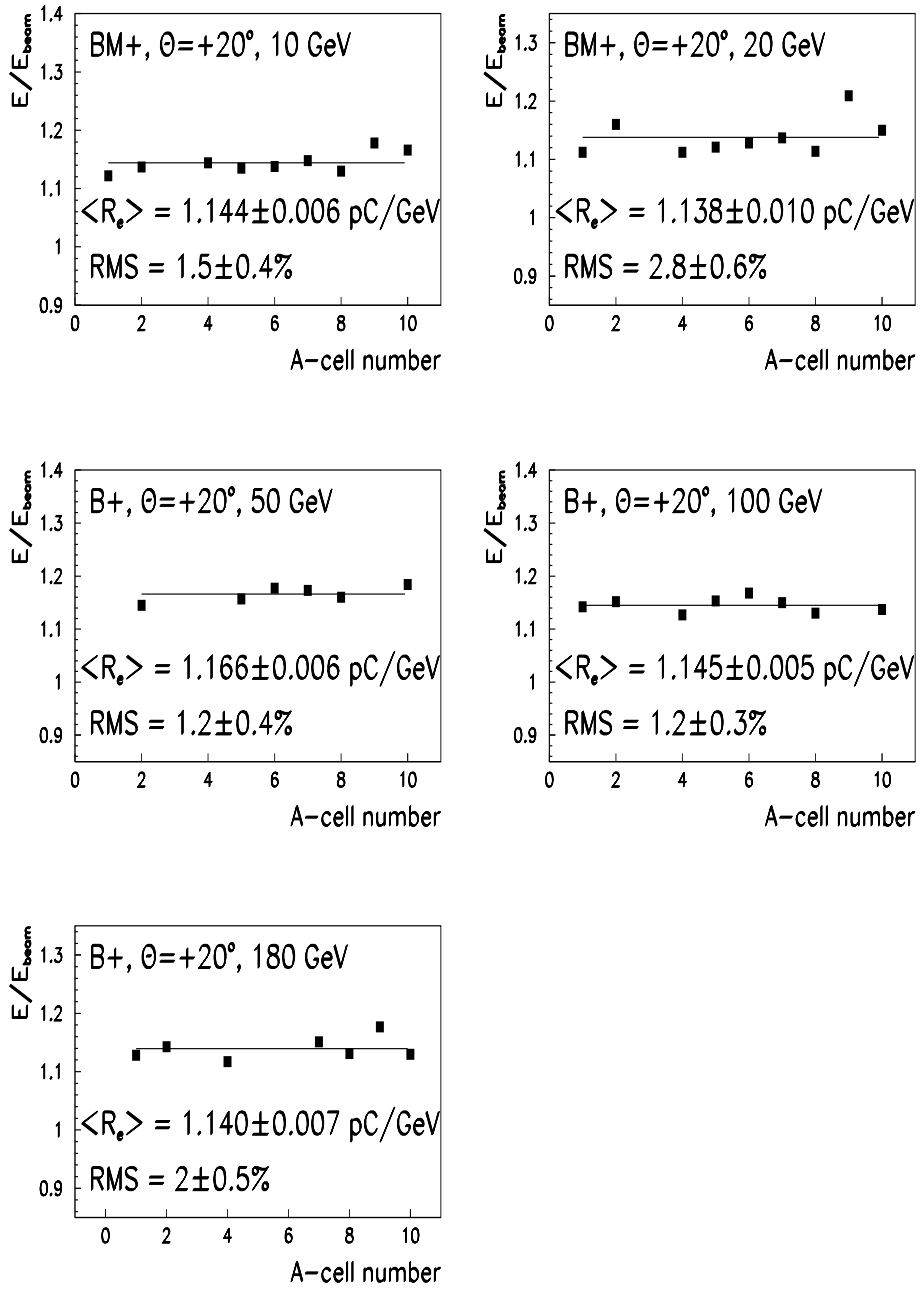

Figure 12: The calibration constants for the A-cells of BM+ for $\theta = 20^{o}$.

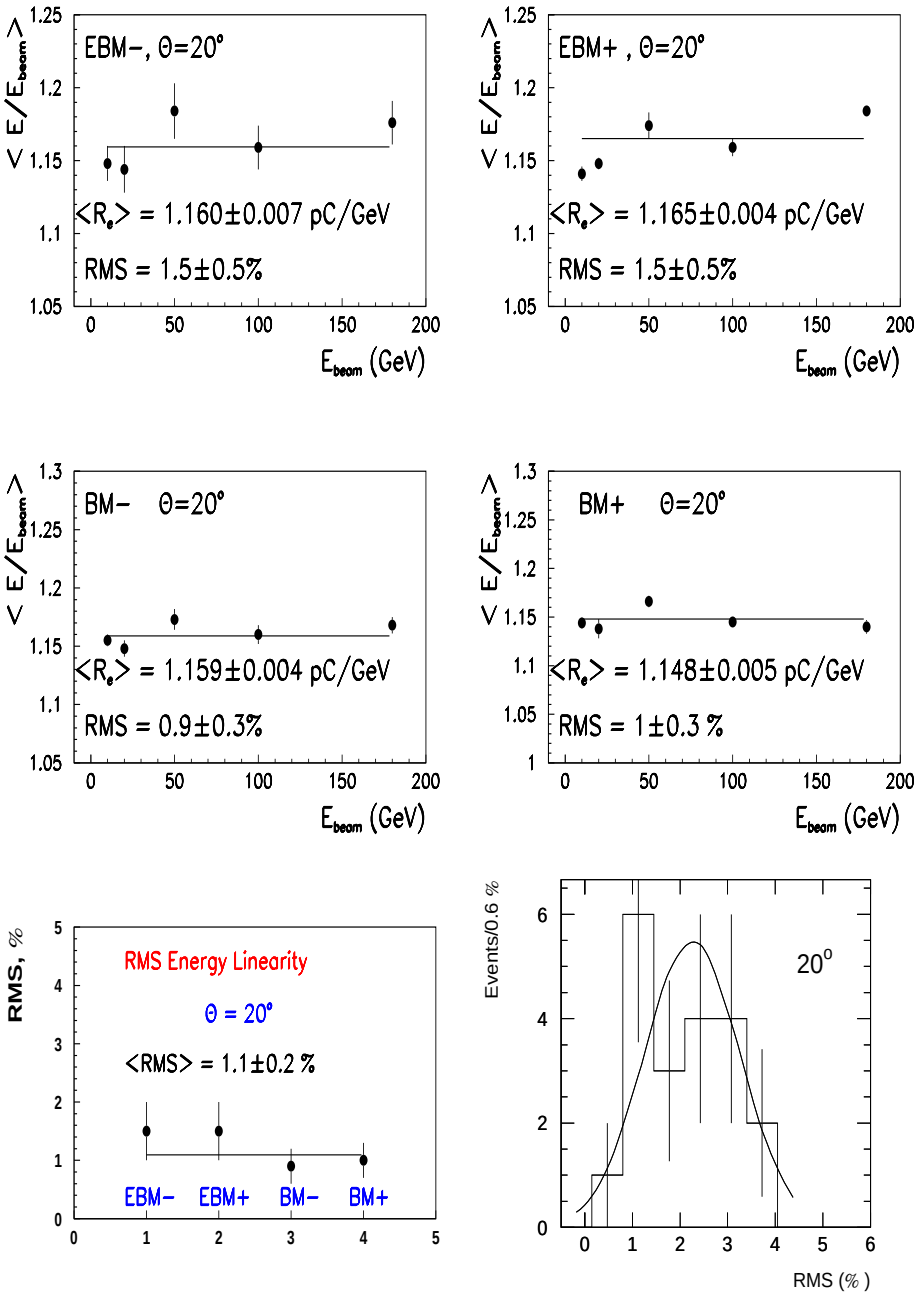

Figure 13: The calibration constants averaged over cells for BM± and EBM± at $\theta = 20^o$ as a function of energy (top, middle). The RMS values of energy linearity (down-left). The distribution of the RMS values of uniformity (down-right).

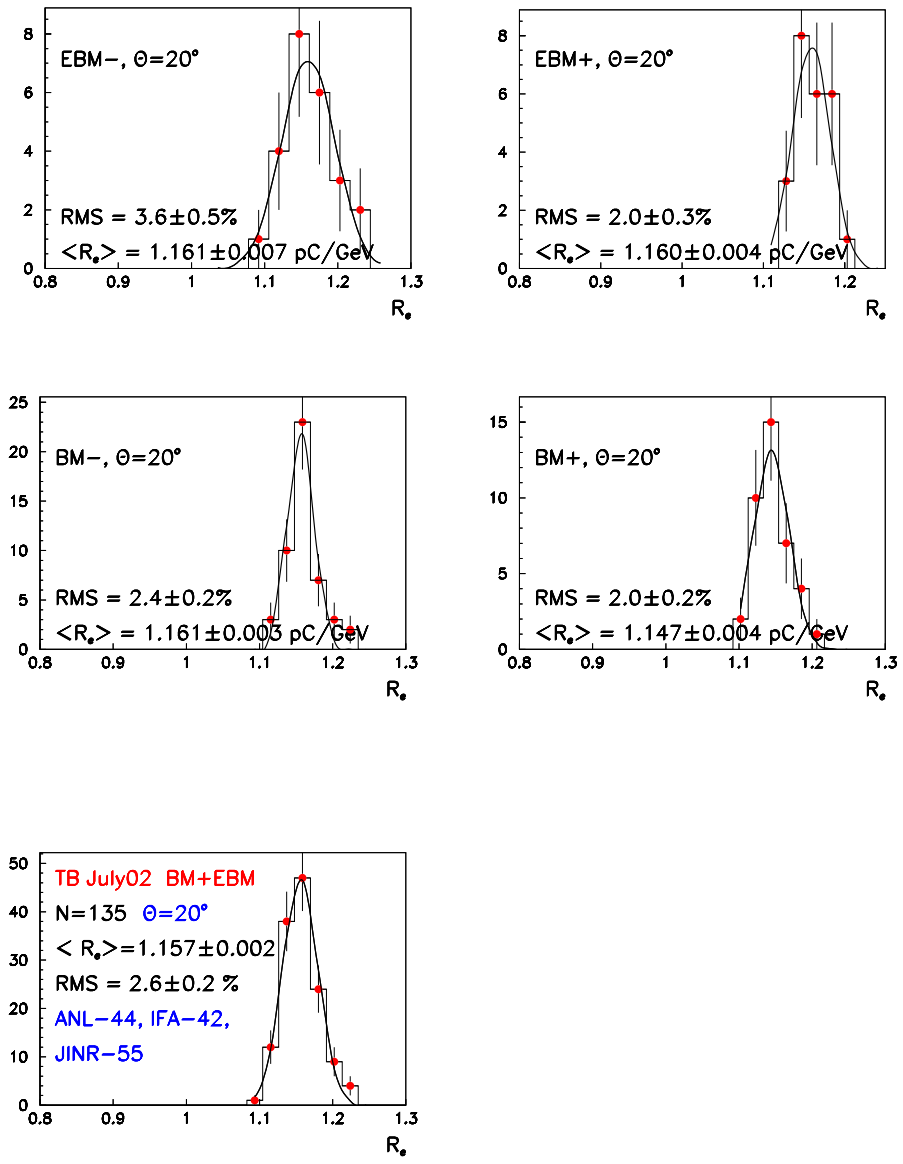

Figure 14: The distributions of the calibration constants of EBM− (up-left), EBM+ (up-right), BM− (middle-left) and BM+ (middle-right), and for all modules (down-left) for all energies at $\theta = 20^o$.

(right-down)). The average and RMS values for this distribution are equal $\langle R_e \rangle = 1.149 \pm 0.004$ pC/GeV , $RMS = 3.0 \pm 0.3\%$. The RMS value became smaller and coincided within errors with the 20^o one.

6.3 Tilerow-scan at $\theta = 90^o$

Figs. 20–23 show the obtained calibration constants for tilerow-scan at $\theta = 90^o$ of EBM−, EBM+, BM−, BM+ modules for different energies as a function of a tilerow number. Tables 5–6 give the corresponding numerical values. Fig. 24 (down-right) demonstrates the distribution of the uniformity RMS values. The mean value is equal to $(4.5 \pm 0.3)\%$. Fig. 24 (top, middle) shows the energy dependencies the constants averaged over cells. Fig. 24 (down-left) gives the RMS values of energy non-linearity for separate modules. The mean RMS value is equal $(1.7 \pm 0.3)\%$. Fig. 25 demonstrates the distributions of the calibration constants for tilerow-scan for all energies for EBM− , EBM+, BM− and BM+ modules separately, and for all modules together. The numerical values of means and RMS values of these distributions are given in Table 7. The average value of the summary distribution (Fig. 25 (down)) is equal to $\langle R_e \rangle = 1.196 \pm 0.005$ pC/GeV and $RMS = 5.7 \pm 0.3\%$.

7 Calibration of high and low gain channels

The Tile Calorimeter digitizer system uses the bi-linear approach with two separate high (for energies less or equal than 20 GeV) and low (for energies more than 20 GeV) gain channels [21].

The PMT signal after the shaper is split in two ways: the first one (for energies more than 20 GeV) is feed directly to the input of the ADC (low gain), while the second (for energies less or equal 20 GeV) is first amplified and then feed to the same type of ADC (high gain). The amplification factor between the low and high gains is set about 64.

Fig. 27 shows the distributions of the calibration constants for the high gain (left) and low gain (right) channels for the flat filter method. The numerical values of the averages and differences between the corresponding averages are given in Table 8. As can be seen, the mean values for the high gain channel calibration constants are less than for

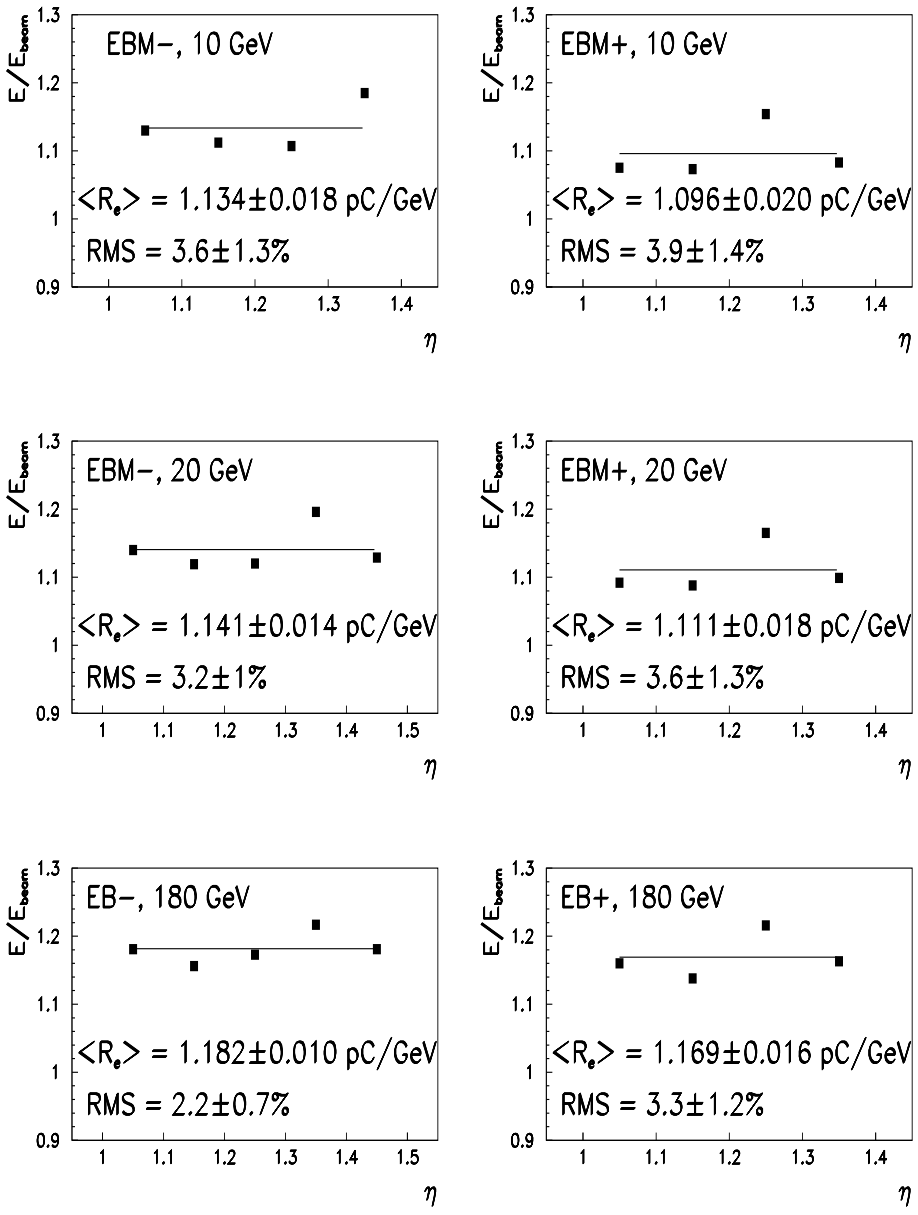

Figure 15: The calibration constants as a function of η for EBM− (left) and EBM+ (right).

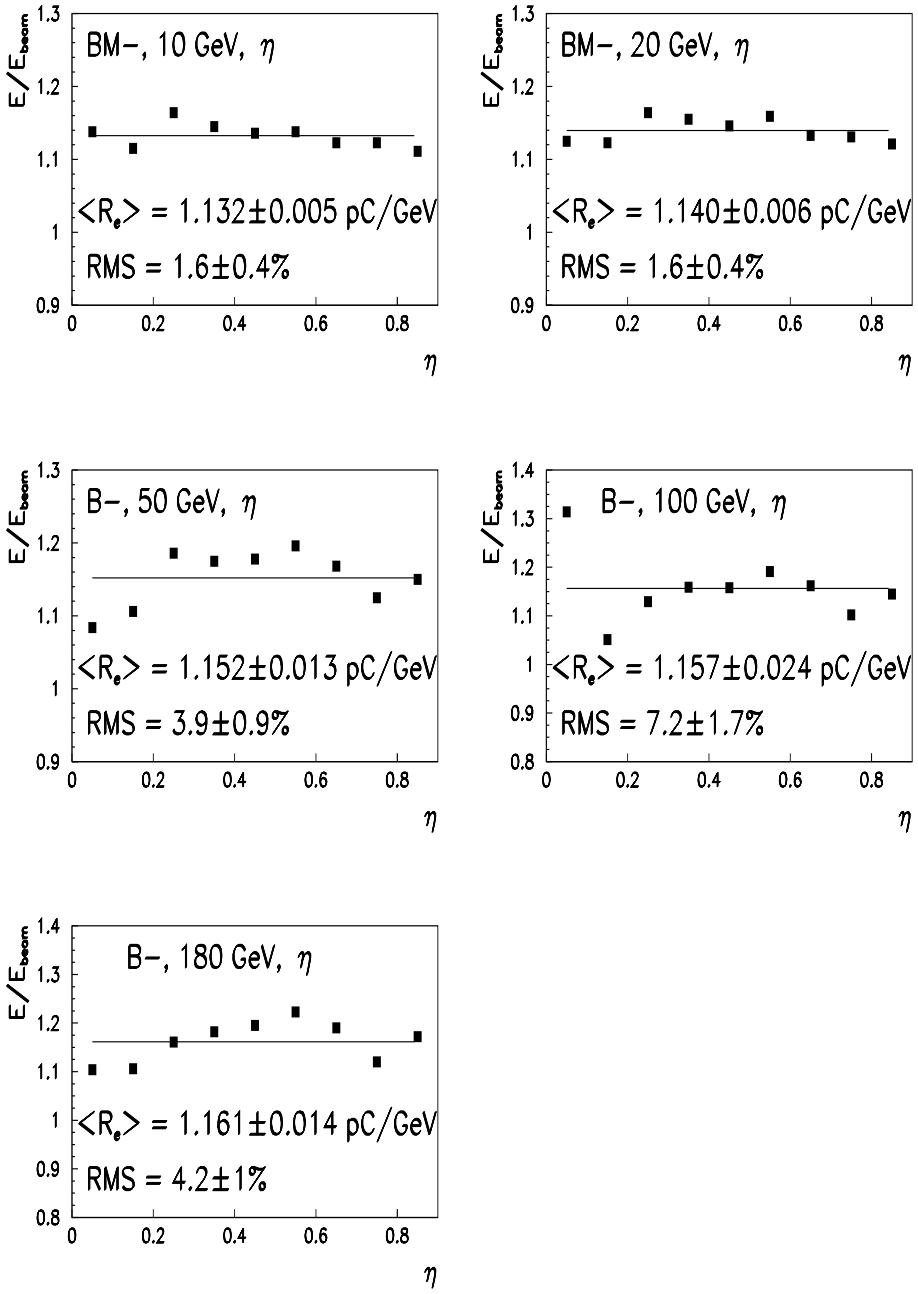

Figure 16: The calibration constants of BM− for η scan.

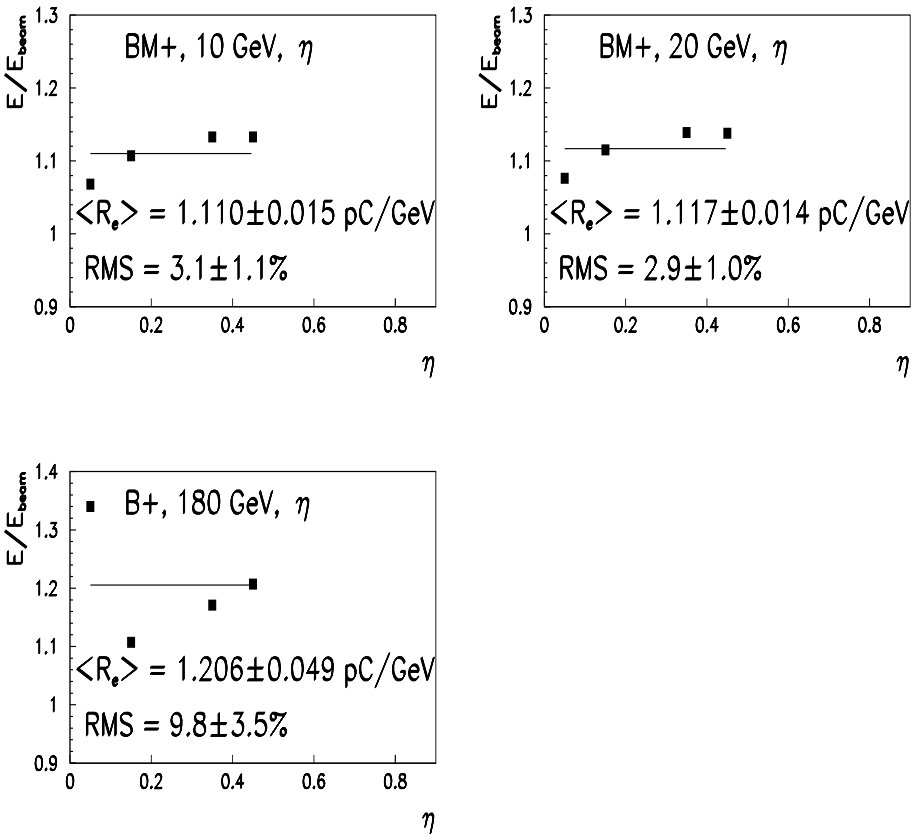

Figure 17: The calibration constants of BM+ for η scan.

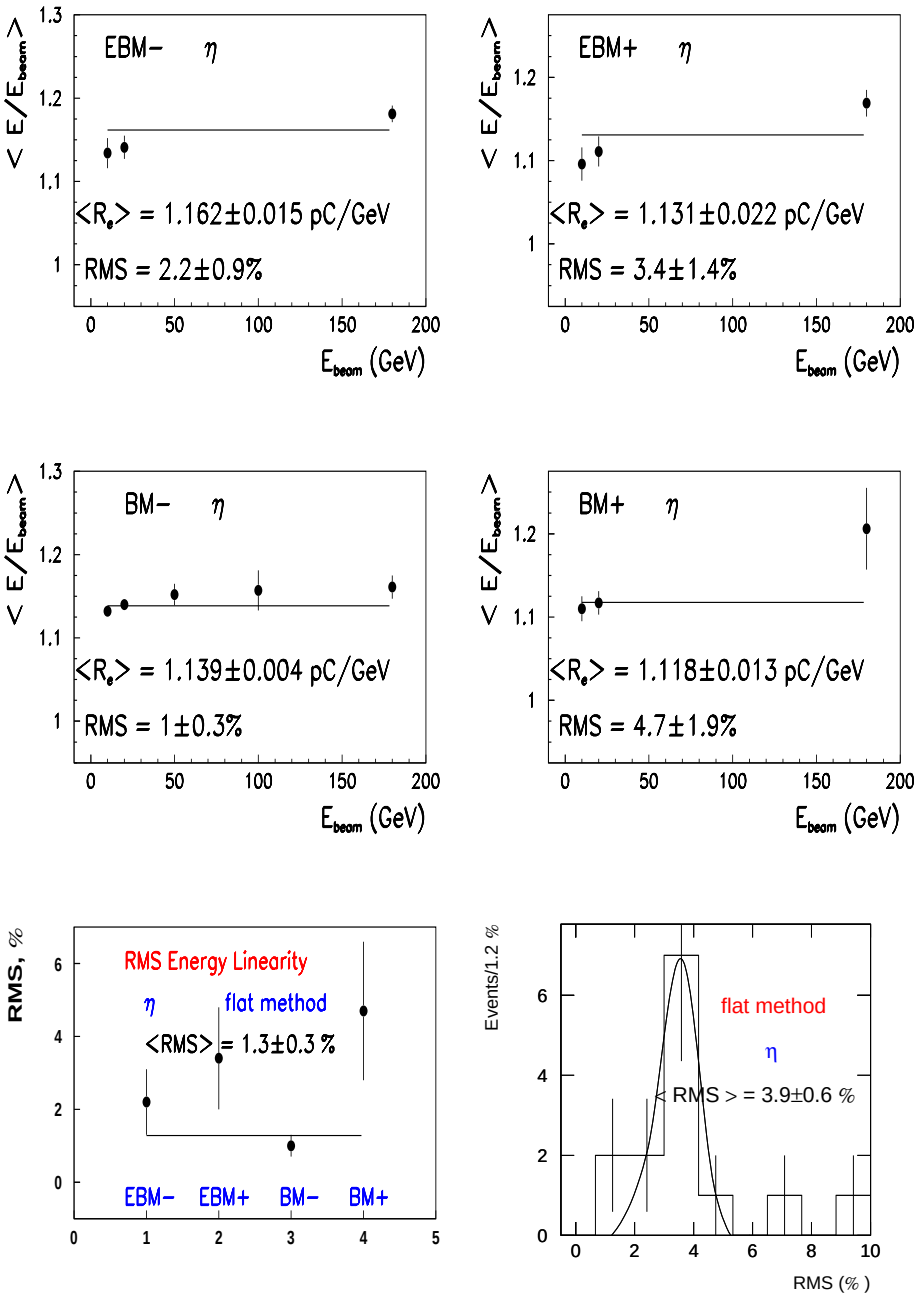

Figure 18: The calibration constants averaged over the η values for BM$\pm$ and EBM$\pm$ as a function of energy (up, middle). The RMS values of energy linearity (down-left). The distribution of the uniformity RMS values (down-right).

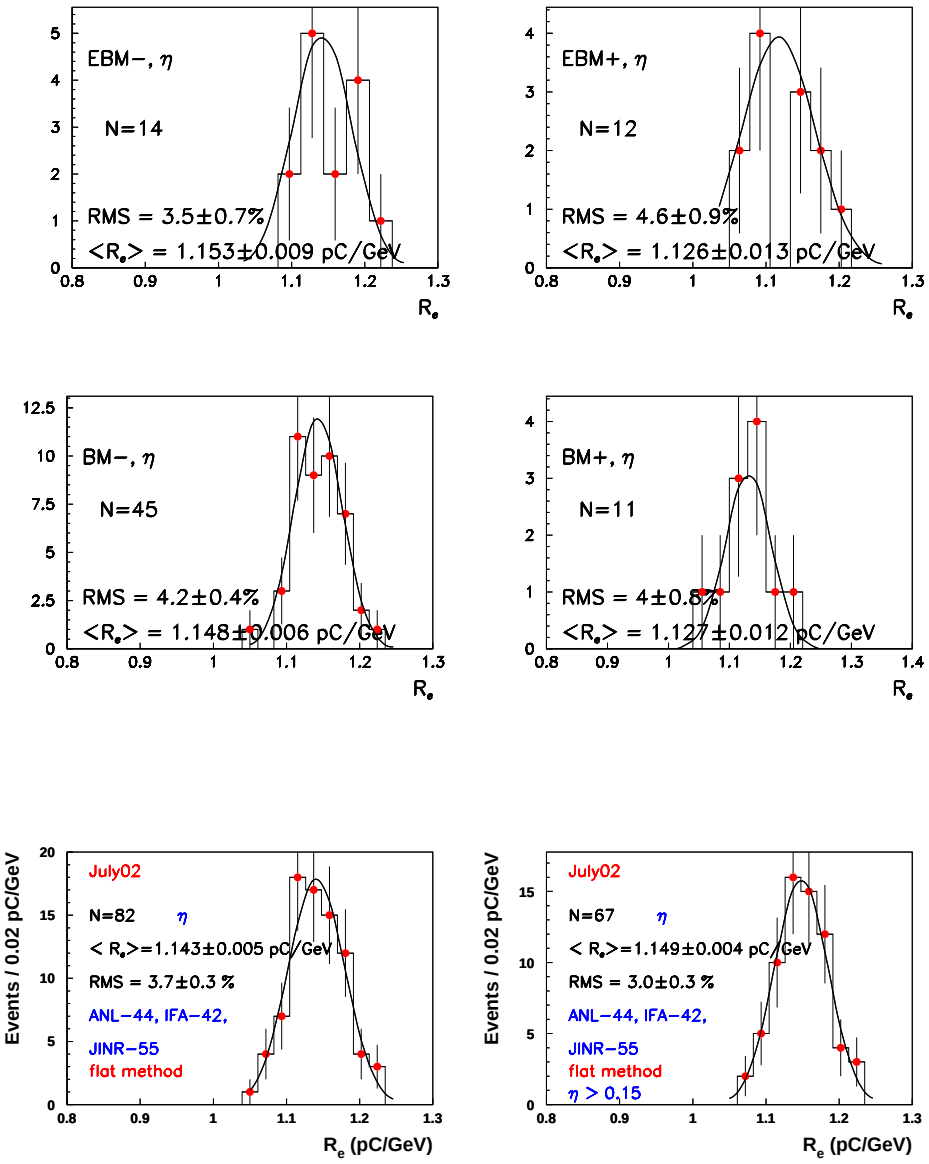

Figure 19: The distributions of the calibration constants for the η scan of EBM− (up-left), EBM+ (up-right), BM− (middle-left) and BM+ (middle-right), for all modules for all energies for all η values (down-left) and for $\eta > 0.15$ (down-right).

the low gain ones. These differences vary from -0.018±0.004 for $\theta = 20^o$ to -0.052±0.008 for $\theta = 90^o$.

8 Uniformity of the calibration constants

Figs. 13, 18, 24 (down-right) show the distributions of the RMS uniformity values of the calibration constants for studied scans. The averages of these distributions are given in Table 8. They vary from 2.1±0.3% for $\theta = 20^o$ to 4.5±0.3% for $\theta = 90^o$. Note that the average tile-to-tile uniformity in a cell obtained on the basis of Cs data is 6% [22].

9 Summary of the calibration constants for all scans

The average calibration constants and RMS (%) values for EBM− , EBM+, BM− and BM+ separately, and for all modules together for A-cells scan at $\theta = 20^o$, η scan and tilerows scan at $\theta = 90^o$, extracted from distributions shown in Figs. 26, are given in Table 7. The average calibration constant for $\theta = 20^o$ is of (3.4 ± 0.4)% smaller the one for $\theta = 90^o$. This fact can be explained by the transition effect [23, 24, 25], decreasing of the e/mip ratio (mip is a calorimeter response to minimum ionizing particle) with decreasing of the sampling frequency (the number of active layers per radiation length of the calorimeter).

10 Conclusions

- With the aim of establishing of an electromagnetic energy scale of the ATLAS Tile calorimeter and understanding of performance of the calorimeter to electrons 12% of modules have been exposed in electron beams with various energies by three possible ways: cell-scan at $\theta = 20^o$ at the centers of the front face cells, η-scan and tilerow scan at $\theta = 90^o$ for the module side cells.

- We have extracted the electromagnetic energy calibration constants of the ANL-44, IFA-42 and JINR-55 modules of the ATLAS Tile Calorimeter at energies E = 10, 20, 50, 100 and 180 GeV and

$\theta = 20^o$ and 90^o and η scan from the July 2002 testbeam run data using the flat filter method for the PMT signal reconstruction.

- The average calibration constants equal to $\langle R_e \rangle = 1.157 \pm 0.002$ pC/GeV, $RMS = 2.6 \pm 0.2\%$ for $\theta = 20^o$, $\langle R_e \rangle = 1.196 \pm 0.005$ pC/GeV, $RMS = 5.7 \pm 0.3\%$ for $\theta = 90^o$, and $\langle R_e \rangle = 1.143 \pm 0.005$ pC/GeV, $RMS = 3.7 \pm 0.3\%$ for all η-scan. For $\eta > 0.15$ region the average and RMS values are equal to $\langle R_e \rangle = 1.149 \pm 0.004$, $RMS = 3.0 \pm 0.3\%$.

- The observed variation of calibration constants ($RMS \simeq 3.0\%$) for A-cell and η scans probably means that it is necessary to determine own calibration constant for each cell in order to achieve the 1% accuracy of the absolute energy scale of hadronic jets.

- The average calibration constant for $\theta = 20^o$ is of $(3.4 \pm 0.4)\%$ smaller the one for $\theta = 90^o$. This fact can be explained by the transition effect, decreasing of the e/mip ratio with decreasing of the sampling frequency.

- The average RMS ununiformity values are equal to $(2.1 \pm 0.3)\%$ for the cell-to-cell uniformity, $(3.9 \pm 0.6)\%$ for η- scan and $(4.5 \pm 0.3)\%$ for tilerows.

- The RMS weighted averages of energy non-linearity are equal to $(1.1 \pm 0.2\%)$ for $\theta = 20^o$, $(1.3 \pm 0.3\%)$ for η-scan, and $(1.7 \pm 0.3\%)$ for $\theta = 90^o$.

11 Acknowledgements

This work is the result of the efforts of many people from the ATLAS TILECAL Collaboration. The authors are greatly indebted to all Collaboration for their test beam setup and data taking.

References

[1] ATLAS Collaboration, ATLAS Technical Proposal, CERN/LHCC/ 94-43, 1994, CERN.

[2] ATLAS Collaboration, ATLAS Detector and Physics Performance, Technical Design Report, ATLAS TDR 15, CERN/LHCC/99-15.

[3] ATLAS Collaboration, ATLAS Detector and Physics Performance, Technical Design Report, ATLAS TDR 14, CERN/LHCC/99-14, p.430.

[4] ATLAS Collaboration, ATLAS Calorimeter Performance, ATLAS TDR 1, CERN/LHCC/96-40, 1996, CERN.

[5] ATLAS Collaboration, ATLAS Tile Calorimeter Technical Design Report, ATLAS TDR 3, CERN/LHCC/96-42, 1996, CERN.

[6] R. Wigmans, Calorimetry, Energy Measurement in Particle Physics, Clarendon Press, Oxford, 2000.

[7] P. Loch, Suggestions for a General Energy Reconstruction Scheme for the ATLAS Calorimeters, ATL-CAL-97-090, CERN, Geneva.

[8] P. Loch, Introduction to Hadronic Calibration of the ATLAS calorimeters, Talk given on the ATLAS Calorimeter Calibration Workshop, December 2004, Tatranska Strba, Slovakia.

[9] J.A. Budagov, Y.A. Kulchitsky, V.B. Vinogradov et al., Electron and Pion Calibrations of the ATLAS TILECAL Modules (September 2001 testbeam), ATL-TILECAL-2003-005, CERN, Geneva; JINR-E1-2003-22 (2003) JINR, Dubna, Russia.

[10] Y.A. Kulchitsky, V.B. Vinogradov, Performances of the ATLAS Hadronic Tile Calorimeter Modules for Electrons and Pions, ATL-TILECAL-2004-013, CERN, Geneva.

[11] Y.A. Kulchitsky, V.B. Vinogradov, Calibration of the Tile calorimeter in the electromagnetic energy scale, Talk given on the ATLAS Calorimeter Calibration Workshop, December 2004, Tatranska Strba, Slovakia.

[12] S. Akhmadalev, Y.A. Kulchitsky, V.B. Vinogradov et al., NIM A480 (2002) 508.

[13] Y.A. Kulchitsky, V.B. Vinogradov, NIM A502 (2003) 708.

[14] M. Bosman, Y.A. Kulchitsky, M. Nessi, Charged Pion Energy Reconstruction in the ATLAS Barrel Calorimeter, ATL-TILECAL-2000-002, CERN, Geneva; JINR-E1-2000-31 (2000) JINR, Dubna, Russia.

[15] Energy reconstruction algorithms, http://tilecal.web.cern.ch /tilecal/Testbeam/documents/method_summary/

[16] R. Teuscher, T. Davidek, Methods of Energy Reconstruction in TileCal, Talk given on the ATLAS TILECAL analysis meeting, June 2003, CERN.

[17] Y.A. Kulchitsky, V.B. Vinogradov, NIM A502 (2003) 775.

[18] P. Amaral, Y.A. Kulchitsky, V.B. Vinogradov et al., NIM A443 (2000) 51.

[19] P. Amaral, Y.A. Kulchitsky, V.B. Vinogradov et al., Eur.Phys.J. C20 (2001) 487.

[20] J.A. Budagov, Y.A. Kulchitsky, V.B. Vinogradov et al., Electron Response and e/h ratio of the ATLAS barrel hadron prototype calorimeter, ATL-TILECAL-96-072, CERN, Geneva; JINR-E1-95-513 (1995) JINR, Dubna, Russia.

[21] S. Berglund et al.,A Digitizer System for the Tile Calorimeter, ATL-TILECAL-97-132, CERN. , Geneva, Switzerland.

[22] R. Leitner, ATLAS Tile Calorimeter, Talk given on the ATLAS plenary meeting, October 2002, CERN.

[23] K. Pinkau, Phys.Rev. B139 (1965) 1548.

[24] R. Wigmans, NIM A259 (1987) 389.

[25] J. del Peso, E. Ros, NIM **A295** (1990) 330.

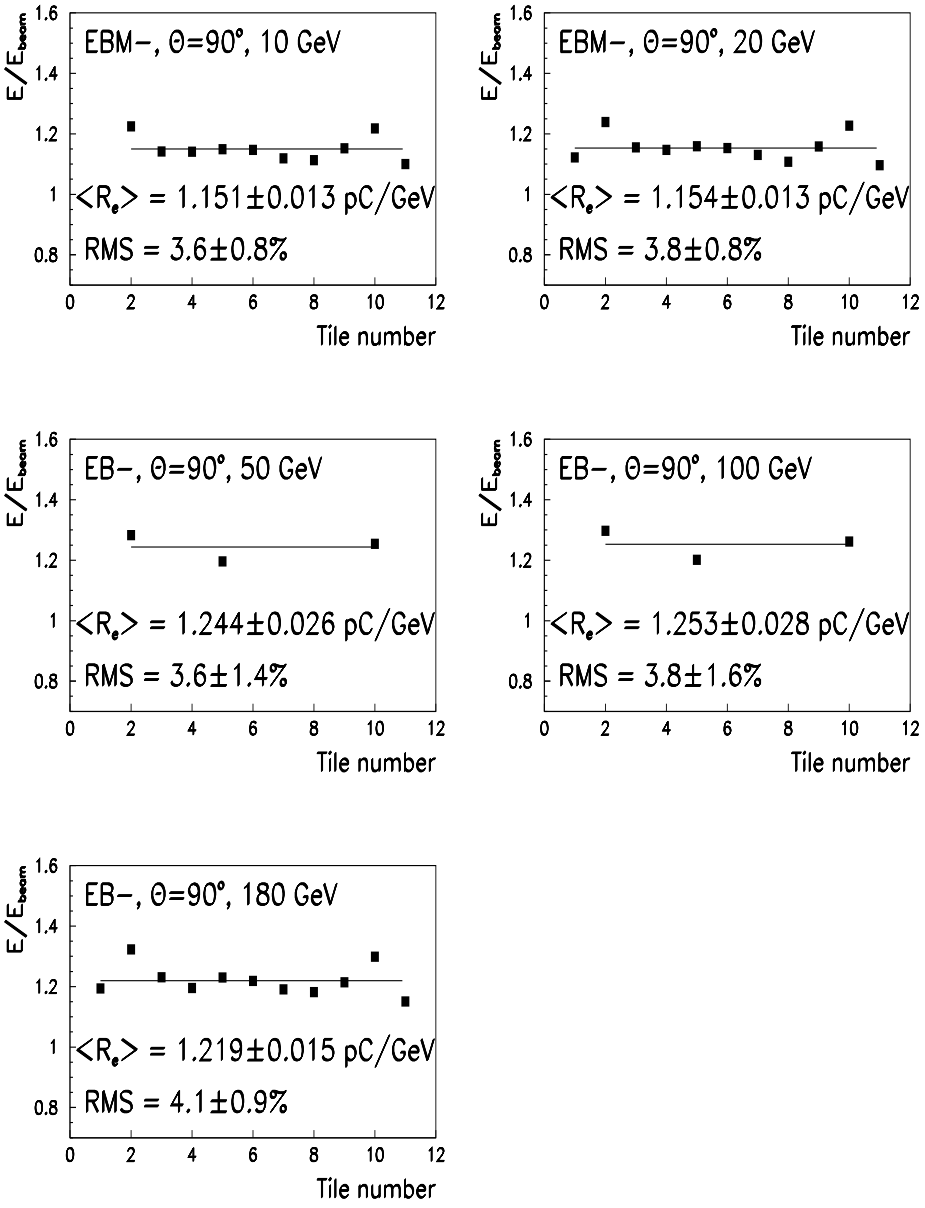

Figure 20: The calibration constants for the tilerows of EBM− for $\theta = 90^o$.

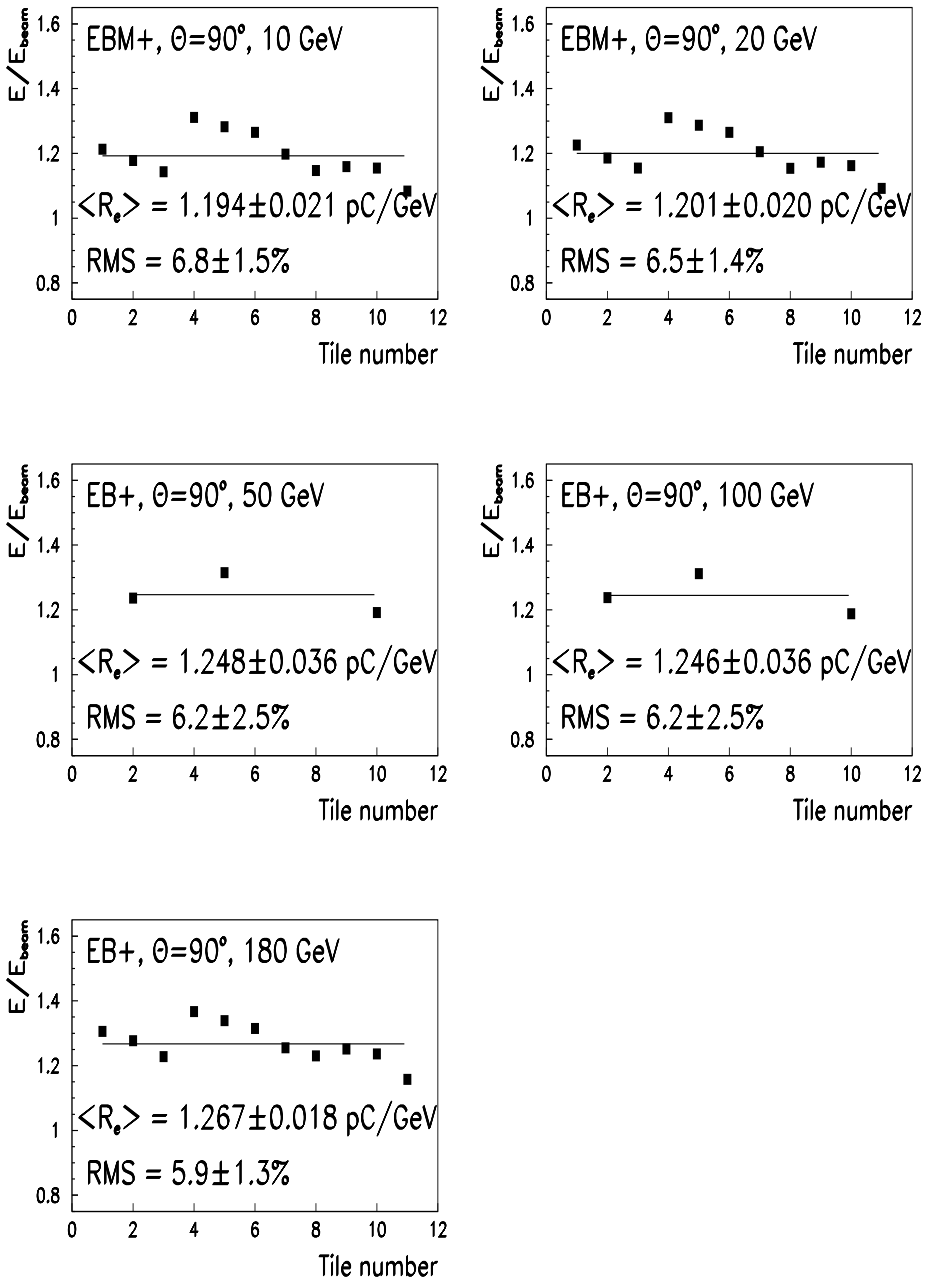

Figure 21: The calibration constants for the tilerows of EBM+ for $\theta = 90^o$.

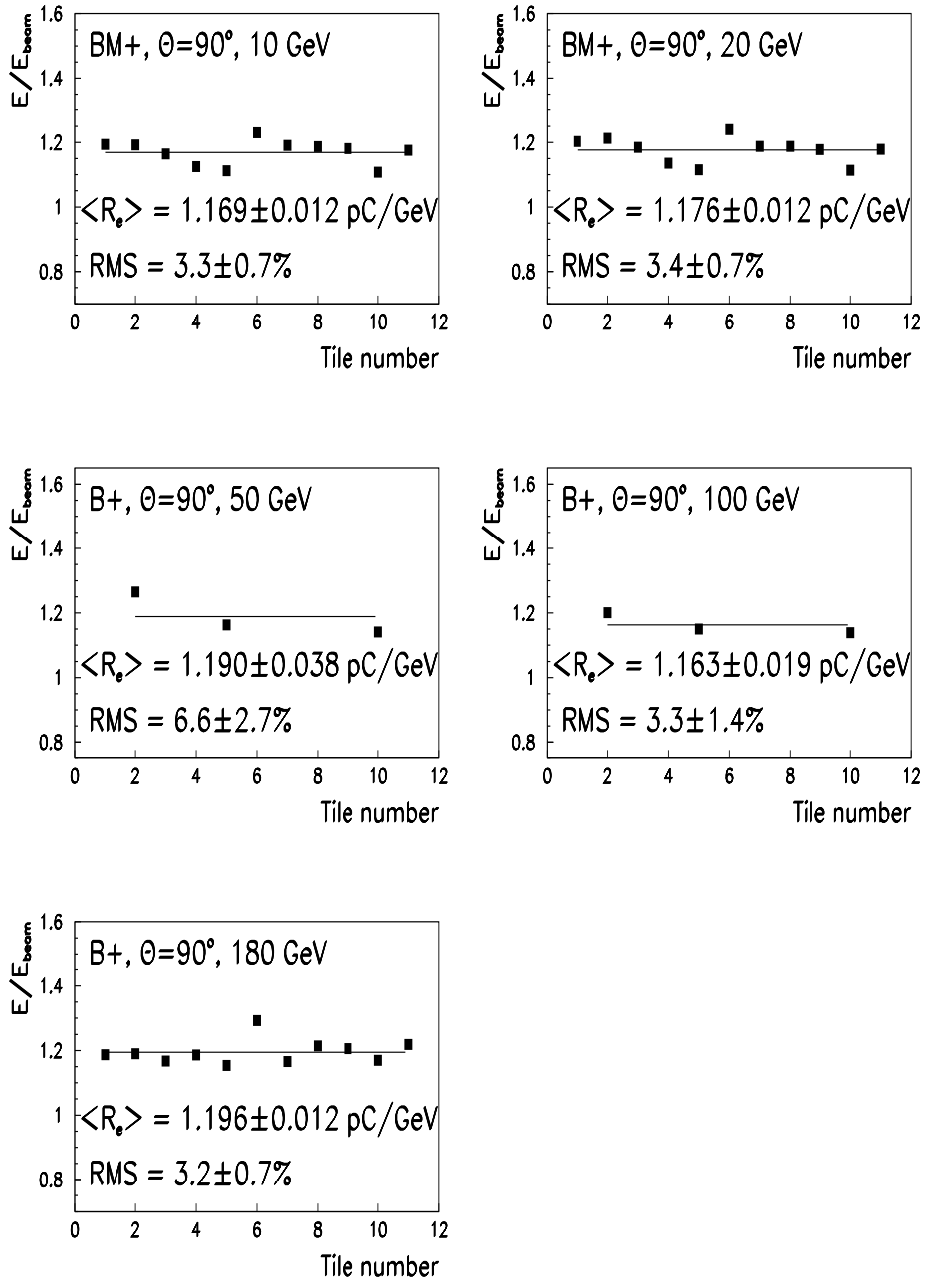

Figure 22: The calibration constants for the tilerows of BM+ for $\theta = 90^{o}$.

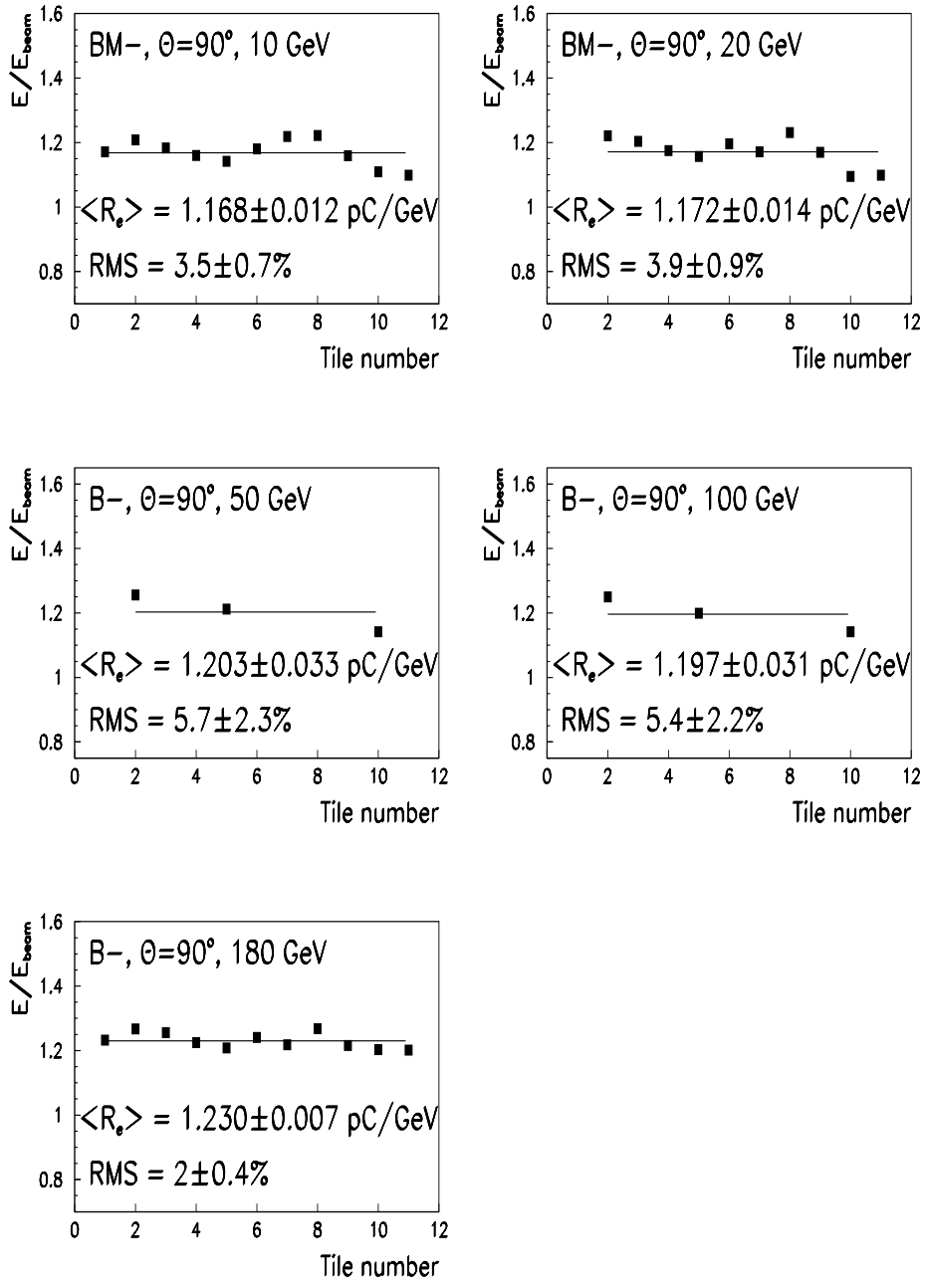

Figure 23: The calibration constants for the tilerows of BM− for $\theta = 90^{o}$.

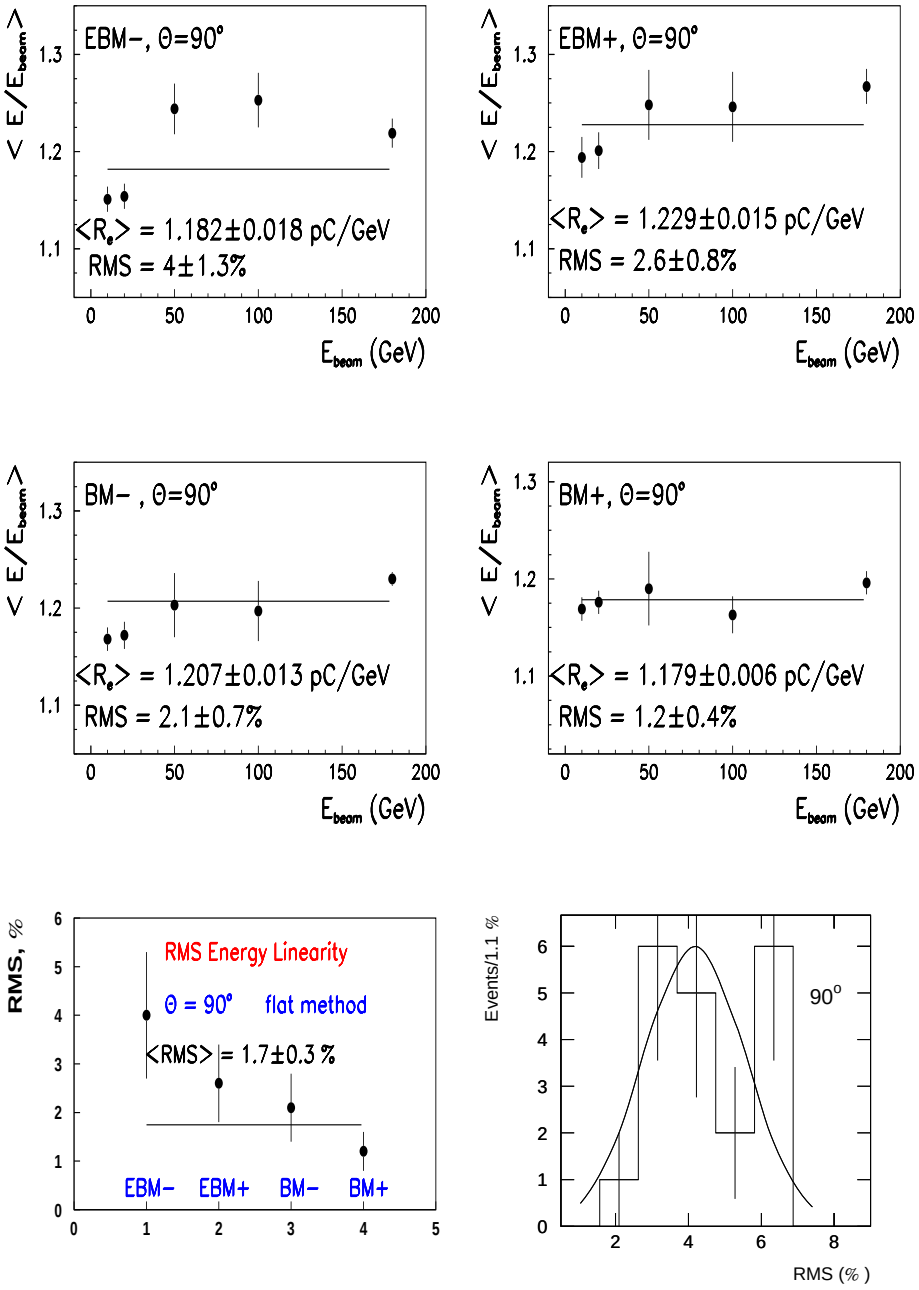

Figure 24: The calibration constants averaged over tilerows for BM± and EBM± at $\theta = 90^o$ as a function of energy (top, middle). The RMS values of energy linearity (down-left). The distribution of the uniformity RMS values (down-right).

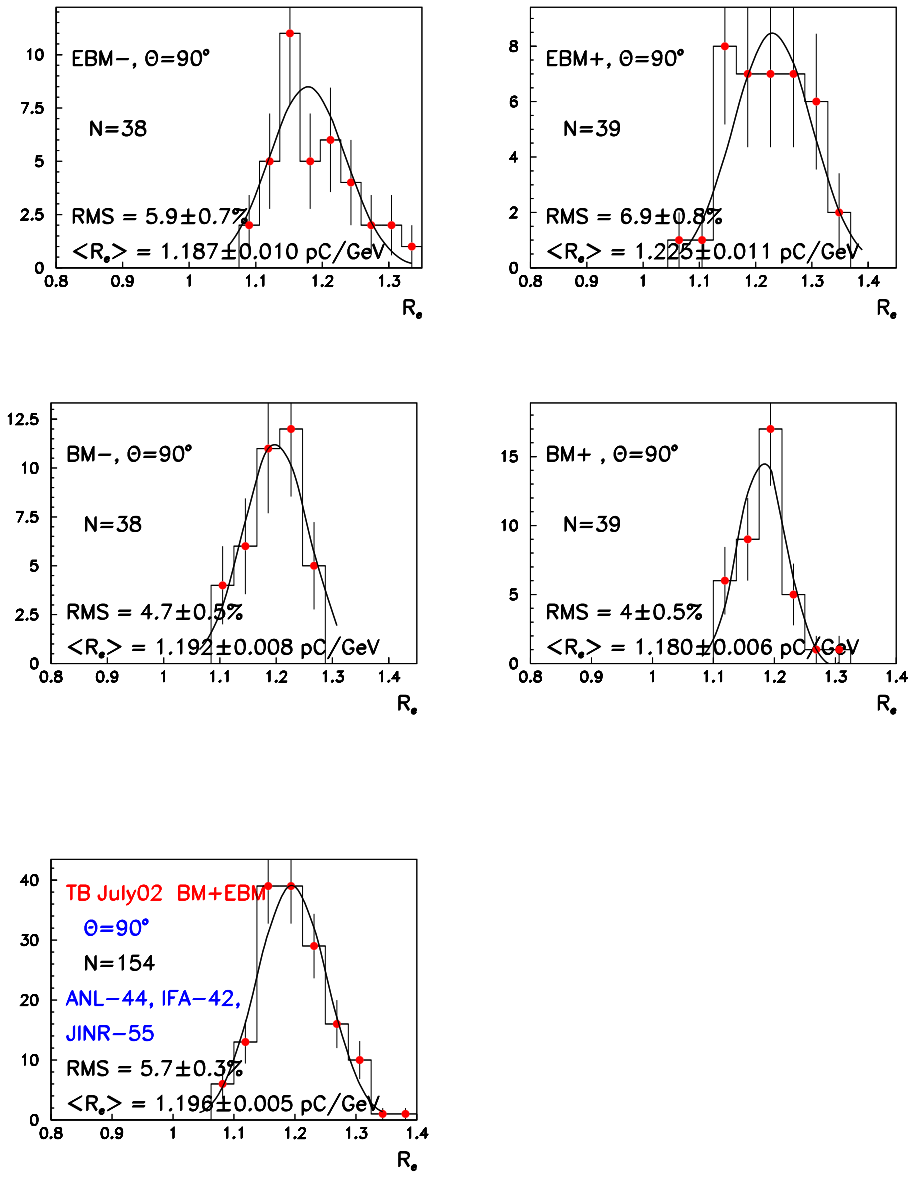

Figure 25: The distributions of the electron calibration constants of EBM− (up-left), EBM+ (up-right), BM− (middle-left) and BM+ (middle-right), and for all modules (down-left) for all energies at $\theta = 90^o$.

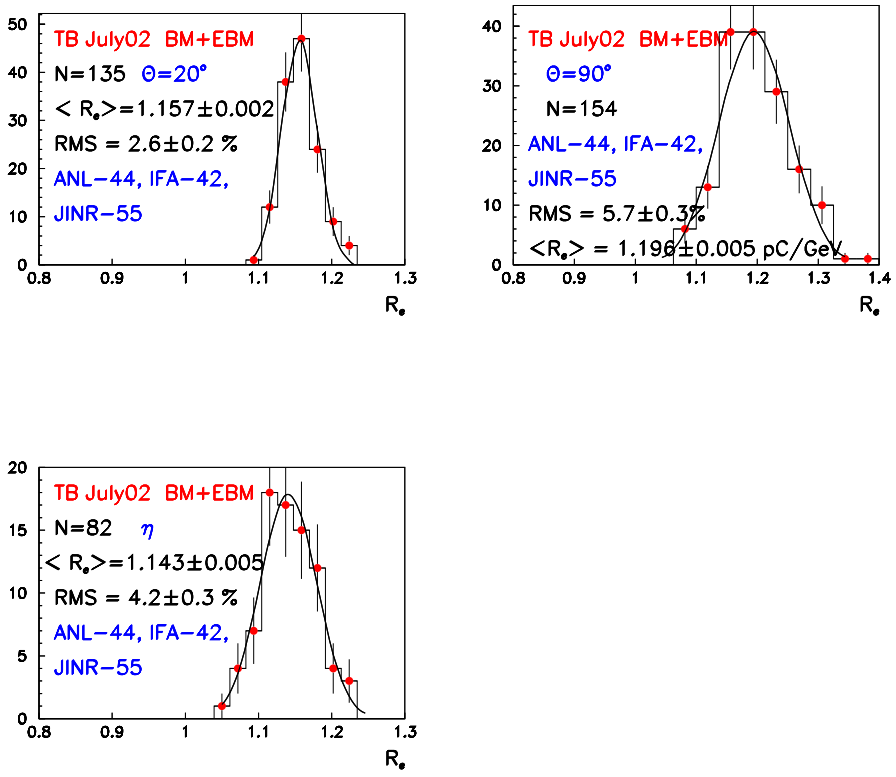

Figure 26: The distributions of the electron calibration constants for $\theta = 20^o$ (up-left), for $\theta = 90^o$ (up-right), for η scan (down-left).

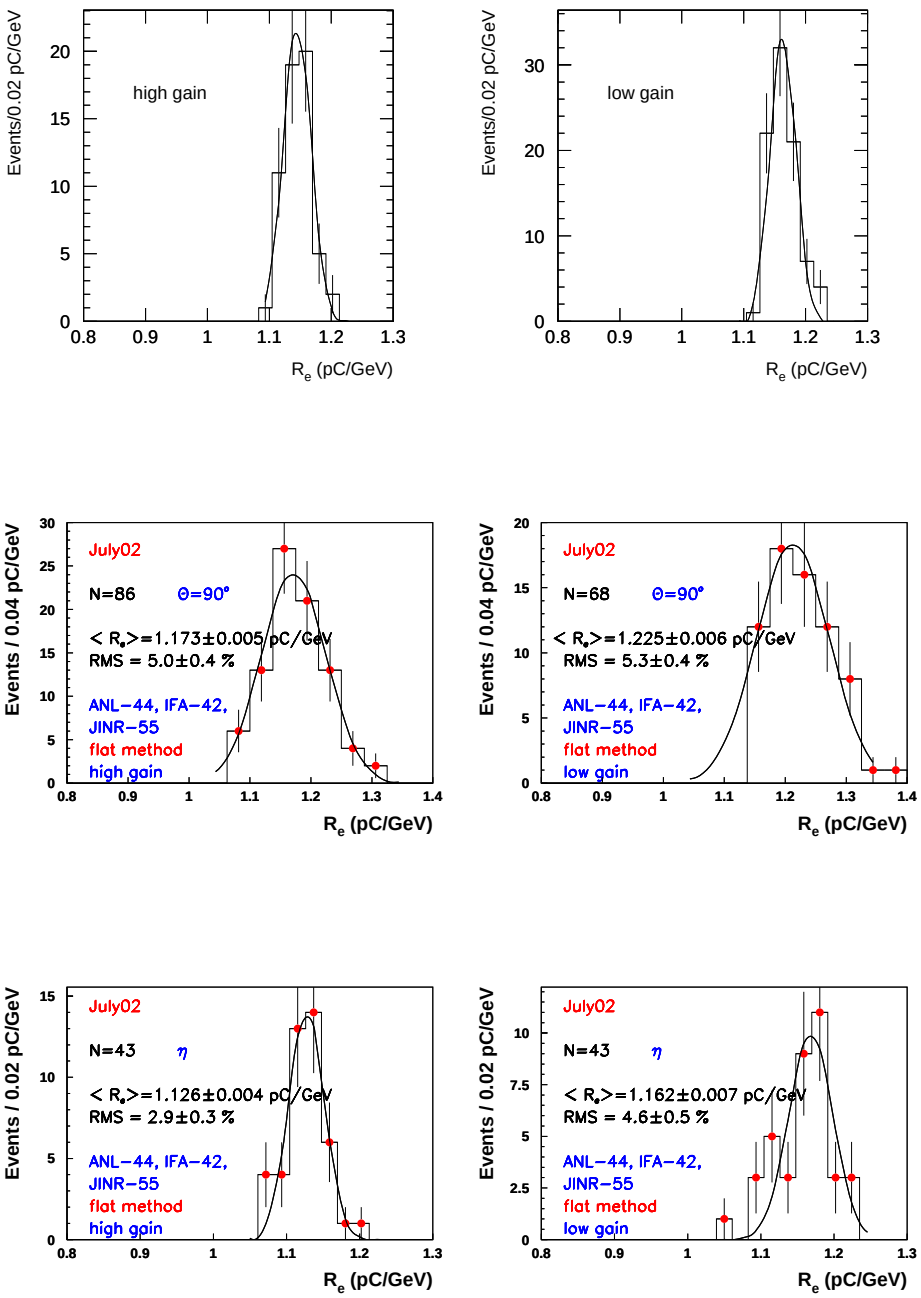

Figure 27: The distributions of the calibration constants for the high gain (left) and low gain (right) for the flat filter method for the JINR-55, ANL-44 and IFA-42 modules for $\theta = 20^o$ (top), $\theta = 90^o$ (middle), and η-scan.

Table 1: The calibration constants (pC/GeV) for the extended barrel modules at $\theta = 20^{\circ}$: EBM+ (IFA-42, A+12 $\div$ A+16) and EBM+ (ANL-44, A$-$12 $\div$ A$-$16). Accuracy of constants is 0.005.

	High Gain		Low Gain		
cell	10 GeV	20 GeV	50 GeV	100 GeV	180 GeV
A+12	1.159	1.161	1.193	1.176	1.191
A+13	1.144	1.146	1.151	1.161	1.179
A+14	1.140	1.146	1.173	1.154	1.180
A+15	1.133	1.137	1.158	1.138	
A+16	1.128	1.149	1.194	1.167	1.186
mean	1.141±0.005	1.148±0.004	1.174±0.009	1.159±0.006	1.184±0.003
mean	1.144±0.003		1.171±0.005		
RMS,%	1.1±0.4	0.9±0.3	2.0±0.6	1.4±0.4	0.6±0.2
RMS,%	1.0±0.2		1.7±0.3		
A$-$12	1.152	1.150	1.196	1.170	1.176
A$-$13	1.181	1.138	1.175	1.154	1.169
A$-$14	1.115	1.120		1.123	1.144
A$-$15	1.103	1.112	1.137	1.138	1.160
A$-$16	1.188	1.201	1.228	1.212	1.231
mean	1.148±0.012	1.144±0.016	1.184±0.019	1.159±0.015	1.176±0.015
mean	1.146±0.01		1.172±0.009		
RMS,%	3.8±1.2	3.5±1.1	3.8±1.3	3.4±1.1	3.3±1.0
RMS,%	3.4±0.8		3.4±0.6		

Table 2: The calibration constants (pC/GeV) for the JINR-55 barrel module at $\theta = 20^o$. Accuracy of constants is 0.005.

	High Gain		Low Gain		
cell	10 GeV	20 GeV	50 GeV	100 GeV	180 GeV
A+1	1.122	1.112		1.146	1.128
A+2	1.137	1.160	1.145	1.152	1.143
A+3					
A+4	1.144	1.112		1.127	1.117
A+5	1.135	1.121	1.157	1.153	
A+6	1.138	1.128	1.177	1.168	
A+7	1.148	1.137	1.173	1.150	1.151
A+8	1.130	1.114	1.160	1.130	1.131
A+9	1.178	1.209			1.177
A+10	1.166	1.150	1.184	1.137	1.130
mean	1.144±0.006	1.138±0.010	1.166±0.006	1.145±0.005	1.140±0.007
mean	1.145±0.005		1.152±0.004		
RMS,%	1.5±0.4	2.8±0.6	1.2±0.4	1.2±0.3	2.0±0.5
RMS,%	1.0±0.4		1.8±0.3		
A−1	1.160	1.154	1.164	1.149	1.148
A−2	1.123	1.117	1.165	1.137	1.139
A−3	1.158	1.156	1.178	1.144	1.178
A−4	1.169	1.164	1.174	1.181	1.165
A−5	1.167	1.166	1.164	1.185	1.204
A−6	1.178	1.185	1.222	1.205	1.198
A−7	1.156	1.141	1.156	1.157	1.157
A−8	1.164	1.155	1.222	1.138	1.163
A−9	1.135	1.128	1.153	1.144	1.164
A−10	1.140	1.119	1.130		
mean	1.155±0.005	1.148±0.007	1.173±0.009	1.160±0.008	1.168±0.007
mean	1.152±0.004		1.167±0.005		
RMS,%	1.7±0.4	2.2±0.5	2.9±0.6	2.4±0.6	2.2±0.5
RMS,%	1.9±0.3		2.5±0.3		

Table 3: The calibration constants (pC/GeV) for the two extended barrel modules for various η: EBM+ (IFA-42) for $\eta > 0$ and EBM− (ANL-44) for $\eta < 0$.

	High Gain		Low Gain
η	10 GeV	20 GeV	180 GeV
1.05	1.075	1.092	1.160
1.15	1.073	1.088	1.138
1.25	1.154	1.165	1.216
1.35	1.083	1.099	1.163
mean	1.096±0.020	1.111±0.018	1.169±0.016
mean	1.103± 0.010		1.169±0.016
RMS,%	3.9±1.4	3.6±1.3	3.3±1.2
RMS,%	3.6 ± 0.9		3.3±1.2
−1.05	1.130	1.140	1.181
−1.15	1.112	1.119	1.156
−1.25	1.107	1.120	1.173
−1.35	1.185	1.196	1.217
−1.45		1.129	1.181
mean	1.134±0.018	1.141±0.014	1.182±0.010
mean	1.138± 0.010		1.182±0.010
RMS,%	3.6±1.3	3.2±1	2.2 ±0.7
RMS,%	3.2 ± 0.7		2.2 ±0.7

Table 4: The calibration constants (pC/GeV) for the BM± (JINR-55) barrel module for η scan. Accuracy of constants is 0.005.

	High Gain		Low Gain		
η	10 GeV	20 GeV	50 GeV	100 GeV	180 GeV
−0.05	1.138	1.125	1.084	1.314	1.104
−0.15	1.115	1.123	1.106	1.051	1.106
−0.25	1.164	1.164	1.186	1.129	1.161
−0.35	1.145	1.155	1.175	1.159	1.182
−0.45	1.136	1.146	1.178	1.158	1.195
−0.55	1.138	1.159	1.196	1.191	1.223
−0.65	1.123	1.133	1.168	1.162	1.190
−0.75	1.123	1.131	1.125	1.102	1.120
−0.85	1.111	1.121	1.150	1.145	1.172
mean	1.132±0.005	1.140±0.006	1.152±0.013	1.157±0.024	1.161±0.014
mean	1.136± 0.004		1.157± 0.010		
RMS,%	1.6±0.4	1.6±0.4	3.9±0.9	7.2±1.7	4.2±1
RMS,%	1.6 ± 0.3		5.1± 0.7		
+0.05	1.068	1.076			1.340
+0.15	1.107	1.115			1.107
+0.25					
+0.35	1.133	1.139			1.171
+0.45	1.133	1.138			1.207
mean	1.110±0.015	1.117±0.014			1.206±0.049
mean	1.113±0.010		1.206±0.049		
RMS,%	3.1±1.1	2.9±1.0			9.8±3.5
RMS,%	2.8± 0.7		9.8±3.5		

Table 5: The calibration constants (pC/GeV) for the extended barrel modules at $\theta = 90^o$: EBM$-$ (IFA-42, T+1 $\div$ T+11) and EBM+ (ANL-44, T$-$1 $\div$ T$-$11).

	High Gain		Low Gain		
cell	10 GeV	20 GeV	50 GeV	100 GeV	180 GeV
T+1	1.213	1.226			1.306
T+2	1.178	1.186	1.236	1.238	1.277
T+3	1.143	1.155			1.228
T+4	1.311	1.310			1.367
T+5	1.282	1.287	1.315	1.312	1.339
T+6	1.265	1.265			1.315
T+7	1.198	1.205			1.255
T+8	1.147	1.154			1.230
T+9	1.159	1.173			1.251
T+10	1.155	1.162	1.192	1.188	1.236
T+11	1.084	1.092			1.158
mean	1.194±0.021	1.201±0.020	1.248±0.036	1.246±0.036	1.267±0.018
mean	1.198± 0.014		1.261± 0.014		
RMS,%	6.8±1.5	6.5±1.4	6.2±2.5	6.2±2.5	5.9±1.3
RMS,%	6.5± 1.0		5.7± 1.0		
T$-$1		1.122			1.194
T$-$2	1.225	1.239	1.283	1.297	1.323
T$-$3	1.142	1.155			1.231
T$-$4	1.141	1.147			1.195
T$-$5	1.149	1.159	1.196	1.201	1.230
T$-$6	1.147	1.153			1.219
T$-$7	1.119	1.130			1.191
T$-$8	1.113	1.108			1.182
T$-$9	1.152	1.158			1.214
T$-$10	1.218	1.227	1.254	1.262	1.299
T$-$11	1.100	1.096			1.151
mean	1.151±0.013	1.154±0.013	1.244±0.026	1.253±0.028	1.219±0.015
mean	1.152± 0.009		1.231± 0.012		
RMS,%	3.6±0.8	3.8±0.8	3.6±1.4	3.8±1.6	4.1±0.9
RMS,%	4.2 ± 0.6		4.8± 0.8		

Table 6: The calibration constants (pC/GeV) for the BM± (JINR-55) barrel module at $\theta = 90^o$.

	High Gain		Low Gain		
tile	10 GeV	20 GeV	50 GeV	100 GeV	180 GeV
BM−1	1.171				1.232
BM−2	1.208	1.221	1.256	1.250	1.267
BM−3	1.183	1.204			1.256
BM−4	1.160	1.175			1.225
BM−5	1.142	1.157	1.212	1.199	1.208
BM−6	1.180	1.196			1.241
BM−7	1.219	1.171			1.218
BM−8	1.222	1.231			1.268
BM−9	1.159	1.170			1.216
BM−10	1.109	1.095	1.142	1.142	1.203
BM−11	1.099	1.099			1.201
mean	1.168±0.012	1.172±0.014	1.203±0.033	1.197±0.03	1.230±0.007
mean	1.170± 0.009		1.220± 0.009		
RMS,%	3.5±0.7	3.9±0.9	5.7±2.3	5.4±2.2	2.0±0.4
RMS,%	4.2± 0.6		3.7± 0.6		
BM+1	1.194	1.203			1.187
BM+2	1.192	1.213	1.265	1.201	1.190
BM+3	1.164	1.185			1.167
BM+4	1.125	1.136			1.186
BM+5	1.112	1.115	1.163	1.150	1.154
BM+6	1.230	1.240			1.293
BM+7	1.191	1.188			1.166
BM+8	1.187	1.188			1.214
BM+9	1.181	1.178			1.206
BM+10	1.108	1.114	1.141	1.139	1.170
BM+11	1.176	1.179		1.137	1.219
mean	1.169±0.012	1.176±0.012	1.190±0.038	1.163±0.019	1.196±0.012
mean	1.173± 0.008		1.189± 0.010		
RMS,%	3.3±0.7	3.4 ±0.7	6.6±2.7	3.3±1.4	3.2± 0.7
RMS,%	3.8± 0.6		4.2± 0.7		

Table 7: The average calibration constants and RMS (%) values for A-cells scan at $\theta = 20^o$, η scan and tilerows scan at $\theta = 90^o$.

Module	20^o		η		90^o	
	R_e pC/GeV	RMS %	R_e pC/GeV	$RMS(\%)$ %	R_e pC/GeV	$RMS(\%)$ %
EBM−	1.161±0.007	3.6±0.5	1.153±0.009	3.5±0.7	1.187±0.010	5.9±0.7
EBM+	1.160±0.004	2.0±0.3	1.126±0.013	4.6±0.9	1.225±0.011	6.9±0.8
BM−	1.161±0.003	2.4±0.2	1.148±0.006	4.2±0.4	1.192±0.008	4.7±0.5
BM+	1.147±0.004	2.0±0.2	1.127±0.012	4.0±0.8	1.180±0.006	4.0±0.5
mean	1.157±0.002	2.6±0.2	1.143±0.005	3.7±0.3	1.196±0.005	5.7±0.3

Table 8: The average calibration constants (pC/GeV) for high and low gains, differences between them (Δ), the average RMS ununiformity values, $< RMS_{un} >$ (%), and the weighted averages of energy non-linearities,$< RMS_{en} >$ (%) for $\theta = 20^o$, $\theta = 90^o$ and η scans.

scan	high gain	low gain	Δ	$< RMS_{un} >$	$< RMS_{en} >$
20^o	1.146±0.003	1.164±0.002	-0.018±0.004	2.1±0.3	1.1±0.2
90^o	1.173±0.005	1.225±0.006	-0.052±0.008	4.5±0.3	1.7±0.4
η	1.126±0.004	1.162±0.007	-0.036±0.008	3.9±0.6	1.3±0.3